UC Santa Barbara

UC Santa Barbara Previously Published Works

Title

Organic matter sulfurization and organic carbon burial in the Mesoproterozoic

Permalink

https://escholarship.org/uc/item/8st7368g

Authors

Raven, Morgan Reed
Crockford, Peter W
Hodgskiss, Malcolm SW
et al.

Publication Date

2023-04-01

DOI

10.1016/j.gca.2023.02.020

Peer reviewed

Organic matter sulfurization and organic carbon burial in the Mesoproterozoic

Morgan Reed Raven,[a]* Peter W. Crockford,[b] Malcolm S. W. Hodgskiss,[c] Timothy W. Lyons,[d] Christopher J. Tino,[d] Samuel M. Webb[e]

[a] Dept. of Earth Science, University of California Santa Barbara, Santa Barbara, CA 93106 USA
[b] Woods Hole Oceanographic Institution, Woods Hole MA 02543 USA
[c] Geological Survey of Norway, Trondheim 7040, Norway
[d] Department of Earth and Planetary Sciences, University of California Riverside, Riverside, CA 92521 USA
[e] Stanford Synchrotron Radiation Lightsource, SLAC National Accelerator Lab, Menlo Park CA, 94025 USA
* corresponding author: *raven@ucsb.edu*

Abstract

Throughout the Proterozoic Era, sedimentary organic carbon burial helped set the pace of global oxygenation and acted as a major modulator of atmospheric CO_2 and climate. Although Proterozoic rocks generally contain low concentrations of organic matter (OM), there are key exceptions to this rule, including the relatively OM-rich Arctic Bay shales from Baffin Island, Canada (Bylot Supergroup, Borden Basin, ~1.05 Ga). The mechanisms driving elevated OM concentrations in these and other Proterozoic shales remain poorly understood. In the Mesozoic and Cenozoic, organic matter sulfurization can be a major driver of enhanced OM burial across a range of redox conditions comparable to those inferred for many Proterozoic environments. Therefore, in this study, we evaluate the role of sulfurization in driving OM preservation in the Mesoproterozoic Borden Basin and discuss its relevance to Proterozoic systems in general. We present the first evidence for syngenetic-to-early-diagenetic OM sulfurization in a Proterozoic basin, which begins to fill a several-billion-year gap in our record of organic S across Earth history. We find that OM sulfurization was particularly extensive in shales from a relatively shallow-water section (Alpha River) but less extensive in shales deposited in deeper water (Shale Valley), which is consistent with models that infer sulfidic 'wedges' or O_2-minimum-zone-type structures on shelf margins at least intermittently at this time. At the shallower site, organic S and pyrite are similarly [34]S-depleted and thus likely formed at roughly the same time near the sediment-water interface under conditions previously interpreted to have been ferruginous to intermittently sulfidic. In contrast, at the deeper-water site, large S-isotope differences between pyrite and organic S along with low apparent OM sulfurization intensities indicate that pyrite formation was favored over OM sulfurization during early sedimentation under variable but primarily ferruginous conditions. Although Mesoproterozoic biomass can be substantially sulfurized, indicators of sulfurization intensity are not correlated with OM concentrations, and therefore sulfurization does not appear to have been the primary driver of enhanced OM concentrations in Arctic Bay Formation

40   shales. The link between sulfurization and total OM preservation may have been modulated during the

41   deposition of Arctic Bay Formation shales by differences in iron availability, nutrient cycling, and particle

42   dynamics in the Mesoproterozoic.

43

44   **1. INTRODUCTION**

45

46   Organic carbon burial in marine sediments is a fundamental control on the biogeochemical evolution of

47   Earth, particularly surface environment oxygenation. Integrated across the Proterozoic, the mechanisms

48   influencing rates of organic carbon burial were crucial factors impacting both the size of the surface

49   reservoir of O_2 and the concentration of CO_2 in the atmosphere. Although Proterozoic rocks generally

50   contain low concentrations of total organic carbon (TOC) (Sperling and Stockey, 2018; Woltz et al., 2021),

51   the TOC-rich shales of the Arctic Bay Formation from Baffin Island, Canada, are a notable exception (Kah

52   et al., 2001; Hahn and Turner, 2017). A 100-meter-thick section of the Arctic Bay Formation at Alpha

53   River, for example, contains an average of 4.8 wt% TOC (n=22, range 0.74 to 12.3 wt%) (Hodgskiss et al.,

54   2020). The mechanisms that support enhanced organic carbon burial in deposits like these shales thus have

55   the potential to influence the global balances of carbon and oxygen throughout the Proterozoic.

56

57   Organic carbon burial fluxes depend on both rates of local primary productivity and the efficiency of

58   organic matter (OM) preservation in the environment. Primary productivity was generally low and

59   predominantly cyanobacterial in the Mesoproterozoic (Derry, 2015; Crockford et al., 2018; Duda et al.,

60   2021), although local, riverine or upwelling-derived inputs of phosphate may have supported higher

61   productivity near river mouths or other ocean margin settings (Laakso and Schrag, 2019). Some proportion

62   of this primary productivity was delivered to, and buried in, sediments, through a variety of preservation

63   mechanisms. High organic carbon burial efficiencies (defined here as the proportion of OM exported from

64   the surface ocean that was preserved in underlying sediment) have been proposed to help balance the global

65   carbon cycle across long intervals of Earth history when rates of primary productivity are inferred to have

66   been significantly lower than today (Kipp et al., 2021). Despite their potential importance for Earth's redox

67   evolution, however, the specific mechanisms that may have led to high organic carbon burial efficiency in

68   the Proterozoic remain largely untested.

69

70   The likelihood of OM being preserved over geologic timescales in sediments depends first upon its delivery

71   to sediments for burial, for example within sinking particles. The susceptibility of OM to remineralization

72   by microbial heterotrophs in both particles and sediments can be reduced if OM is associated with mineral

73   surfaces (Hemingway et al., 2019) or chemically transformed into less functionalized, higher-molecular-

74   weight, polymeric materials. Another factor impacting OM burial efficiency is O_2 exposure time (Hartnett

75   et al., 1998), which reflects the redox structure of the local environment. Longer O_2 exposure times and

76   oxic conditions are associated with low burial efficiencies due to thorough breakdown and remineralization

77   by aerobic micro- and macroscopic organisms. Alternatively, anoxic conditions – whether they result from

78 high export productivity, high sedimentation rates, circulation patterns, or other factors – enhance OM

79 preservation efficiency in part because organisms gain less energy from anaerobic metabolisms and grow

80 more slowly (Canfield, 1994; Jin and Bethke, 2005). Although it has not been widely explored in

81 Precambrian systems, anoxic conditions also have the potential to enhance OM preservation through OM

82 sulfurization.

83

84 Sulfurization can occur in anoxic and sulfidic settings, in either the sediments or the water column.

85 Dissolved sulfide (mostly HS^-) and polysulfides (S_x^{2-}) sulfurize organic matter through reactions with

86 certain reactive functional groups that are common in carbohydrates and lipids, including aldehydes and

87 conjugated double bonds (Sinninghe Damsté and de Leeuw, 1990; Kohnen et al., 1991). These reactions

88 increase the S:C ratio of OM beyond that of microbial biomass (0.5–2 mol%, where 1 mol% is defined as

89 S:C = 1:100 mol/mol or a molar ratio of 0.01; Matrai and Eppley, 1989; Chen et al., 1996) and yield

90 polymeric materials that are more likely than their precursors to be preserved over long timescales in

91 sediments and rocks, thereby enhancing OM burial. Accordingly, higher OM S:C ratios are frequently

92 associated with higher OM concentrations in shales (Boussafir et al., 1995; Van Kaam-Peters et al., 1998),

93 with Ocean Anoxic Event 2 in the Cretaceous (94 Mya) serving as a prominent example of this phenomenon

94 (Raven et al., 2019). Modern sites with substantially sulfurized OM (S:C > ~2 mol%) also typically produce

95 sediments with elevated OM concentrations (TOC > 3 wt%). Such environments include intermittently

96 anoxic to sulfidic basins (Werne et al., 2003; Raven et al., 2016) and the anoxic regions of upwelling zones

97 along the Namibian and Peruvian margins (Eglinton et al., 1994; Dale et al., 2009). Although sulfurization

98 reactions affect organic materials, they are abiotic and have the potential to operate similarly at any point

99 in Earth history if sulfurizable precursors are present. Therefore, elevated OM concentrations in

100 Mesoproterozoic shales could, by analogy to Phaneozoic trends, reflect extensive sulfurization. At the same

101 time, sulfurization is just one of several potential mechanisms for OM preservation in shales; for example,

102 substantial amounts of OM can also be protected against microbial degradation by rapid burial and

103 association with clays and other mineral surfaces (Suess, 1973; Ingall and Cappellen, 1990; Hedges and

104 Keil, 1995; Kennedy et al., 2014). Given differences in the redox structure, productivity, and biomass

105 characteristics of Mesoproterozoic basins, the mechanisms driving locally elevated OM concentrations at

106 that time remain an outstanding problem in the Proterozoic.

107

108 Organic sulfurization products can be distinguished from biogenic organic S by their S-isotope composition

109 as well as their redox speciation. Biogenic S is predominantly assimilated from seawater sulfate and

110 approximately matches its S-isotope composition (Trust and Fry, 1992). Seawater sulfate concentrations in

111 the Mesoproterozoic were likely a few millimolar (1.5 – 4.5 mM) (Kah et al., 2004) although estimates

112   range from a few hundred micromolar (Fakhraee et al., 2019) to as high as 6–10 mM (Blättler et al., 2020),

113   compared with 28 mM today. The S-isotope composition of Mesoproterozoic seawater sulfate has been

114   estimated from carbonate-associated sulfate as well as nodular and bedded evaporites (gypsum; $CaSO_4$)

115   from within the same basin as the Arctic Bay Formation, namely the overlying Iqquituq and Angmaat

116   formations (formerly part of the Society Cliffs Formation), which range from +21.5‰ to +36.4‰ (Kah et

117   al., 2001; Crockford et al., 2019). These data represent our best estimate for Mesoproterozoic seawater

118   sulfate and, by extension, phytoplankton biomass $\delta^{34}S$ values. In contrast, sulfide produced during

119   microbial sulfate reduction (MSR) has a distinctively ^{34}S-depleted composition, with $\delta^{34}S$ values that are

120   typically 15–70‰ lower than contemporaneous sulfate (Kaplan and Rittenberg, 1964; Sim et al., 2011).

121   This signal can subsequently be recorded in abiogenic organic sulfur with a relatively small (typically 4–

122   5‰) additional isotope fractionation (Amrani and Aizenshtat, 2004a; Amrani et al., 2008), although

123   substantial inter-compound variability is possible (Raven et al., 2015; Rosenberg et al., 2017; Shawar et al.,

124   2020). The S-isotope composition of sulfide-derived organic S thus generally resembles sulfide and other

125   sulfide-derived phases, most notably pyrite (FeS_2) (Vairavamurthy et al., 1995).

126

127   In the Mesoproterozoic, many shallow marine environments may have been favorable locations for OM

128   sulfurization. Atmospheric O_2 concentrations were likely ~0.1-10% of modern levels, and the deep ocean

129   was largely anoxic, with transient, localized sulfidic conditions on continental shelves (Lyons et al., 2014;

130   Planavsky et al., 2014, 2018; Cole et al., 2016; Stolper and Keller, 2018). Upwelling and weathering-

131   derived sources of nutrients to the continental shelves likely supported enhanced productivity in coastal

132   environments (Laakso and Schrag, 2019). Across the Proterozoic, the deep ocean is thought to have been

133   predominantly ferruginous, meaning that the Eh of the environment was buffered by the Fe^{3+}/Fe^{2+} redox

134   couple (Poulton and Canfield, 2011; Planavsky et al., 2011) and that dissolved Fe^{2+} concentrations may

135   have been high (micromolar). Importantly, however, many redox reconstructions for this time period rely

136   on the iron speciation proxy, which is subject to depositional and diagenetic effects that can in certain cases

137   reduce confidence in its interpretation (Pasquier et al., 2022). There is also growing evidence that the deeper

138   portion of the Proterozoic water column may have been characterized by more dynamic redox conditions

139   than previously suggested, with intermittent oxygenation (Knoll and Sperling, 2014; Zhang et al., 2018;

140   Diamond and Lyons, 2018; Hodgskiss et al., 2020) or nitrogenous conditions, buffered instead by the

141   nitrate/nitrite redox couple (Michiels et al., 2017; Stüeken et al., 2021). The differences between different

142   possible 'flavors' of Proterozoic ocean anoxia – e.g, ferruginous versus nitrogenous versus sulfidic

143   conditions and the dynamic transitions among these end-members – are critically important for organic

144   carbon burial due to their impacts on both the favorability of various metabolic pathways and the activities

145   of different preservation mechanisms for sedimentary organic matter. In terms of the favorability of OM

sulfurization, sulfidic and potentially nitrogenous conditions may provide the conditions necessary to support early OM sulfurization in the water column or near the sediment-water interface. However, elevated concentrations of Fe^{2+} under ferruginous conditions have the potential to react rapidly with any available sulfide to produce iron sulfide solids (primarily FeS and FeS_2) and thus limit the sulfide available for OM sulfurization in the water column.

Here, we present a detailed assessment of the S-isotope compositions and speciation of organic and inorganic sulfur phases in two stratigraphic sections from the late Mesoproterozoic Arctic Bay Formation, which have been interpreted to record a range of oxic, ferruginous, and intermittently sulfidic conditions (Hodgskiss et al., 2020). We use these data to evaluate the mechanisms that contributed to organic matter preservation in the mid-Proterozoic, testing the relationship between organic matter sulfurization and elevated organic carbon preservation in ancient, anoxic oceans. By comparing patterns in the S-isotope compositions of sulfate, pyrite, and organic sulfur, we evaluate the potential locations and pathways of pyrite and organic sulfur formation in the ancient environment and, by extension, its organic carbon cycle and redox structure.

2. MATERIALS AND METHODS

2.1 Geological Context
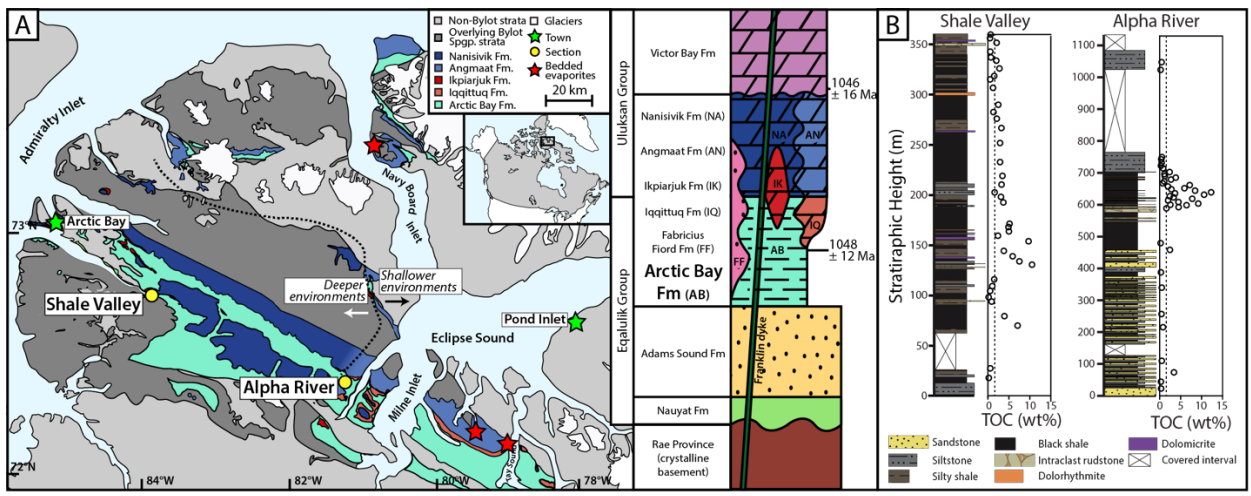
Fig. 1 Site overview, stratigraphy and organic carbon content. Modified from Hodgskiss et al., 2020 figs. 1 and 5. Dotted line on panel 'A' shows the 'deeper' to 'shallower' facies transition as interpreted from the depositional facies of the overlying Angmaat/Iqqittuq/Nanisivik formations (Turner and Kamber,

171   2012). Dashed vertical line in both panels in 'B' shows median late Mesoproterozoic TOC values (Sperling
172   and Stockey, 2018).

173

174   Samples for this study come from the Arctic Bay Formation, Bylot Supergroup, Borden Basin, northern
175   Baffin Island, Nunavut, Canada. Age control is provided by Re-Os dates of 1048 ± 12 Ma for the middle-
176   upper Arctic Bay Formation and 1046 ± 16 Ma for the overlying Victor Bay Formation (Gibson et al.,
177   2018). The Arctic Bay Formation is a thick section (180 – 1130 m, thinning to the northwest; Turner and
178   Kamber, 2012) of OM-rich shales; the lower interval contains repeating shale-silt-sand shallowing-upward
179   packages, and the upper interval contains interbedded black shales, silty shales and silts without regular
180   cyclicity. The Shale Valley section ("T1413"; N72.75133°, W83.84422°) spans 358 m from the lower
181   Arctic Bay to the overlying contact in the Ikpiarjuk Fm. The Alpha River site is a composite of two
182   shallower-water sections ("PWC1405" and "MB1401"; N72.39550°, W81.18947°) spanning 1130 m of
183   stratigraphy from underlying Adams Sound to overlying Iqqittuq Fm. Although both sites record
184   approximately the same time interval, Alpha River and Shale Valley records have not been directly
185   correlated because they are ~90 km apart, are affected by low-angle erosive hiatuses, and lack marker beds
186   (Turner and Kamber, 2012; Hodgskiss et al., 2020). Total carbon, nitrogen, and sulfur contents, bulk N and
187   organic C isotope data, trace element concentrations, and iron speciation for these sections were presented
188   in Hodgskiss et al. (2020).

189

190   The Arctic Bay Formation is underlain by the Adams Sound Formation, a thick (up to 610 m; Long and
191   Turner, 2012) quartz arenite representing shallow marine deposition. Active normal faulting in the basin is
192   thought to have led to rapid subsidence and deposition of Arctic Bay Formation shales, siltstones, and
193   sandstones along a gentle depth gradient, deepening to the present-day northwest (Turner and Kamber,
194   2012). The lower Arctic Bay Formation contains a series of shallowing-upward clastic cycles. In the Alpha
195   River section, which records relatively shallow-water deposition, black shales containing as much as 12.3
196   wt% TOC are concentrated in a roughly 100-m-thick interval in the middle of the formation; these are
197   overlain by layers of black shale and siltstone. The Shale Valley section reflects a deeper environment and
198   is composed of interbedded siltstones and black shales. TOC concentrations in Shale Valley are generally
199   higher in the lower part of the section (averaging 4.8 wt% from 0 – 170 m) and moderate in the upper part
200   (averaging 2.1 wt% from 170 – 351 m) (Hodgskiss et al., 2020). Following the deposition of the Arctic Bay
201   Formation, deposition in the shallower part of the basin is recorded in the Iqquittuq Formation, which
202   reflects a carbonate ramp environment and is composed of interbedded dolomicrite and shale. In the deeper
203   (northwest) part of the basin, the Arctic Bay Formation is overlain by the Ikpiarjuk Formation, consisting
204   of dolostone mounds that may reflect fluid venting along faults (Hahn and Turner, 2017). Carbonates

205 continued to dominate subsequent deposition in both regions. Units overlying the Arctic Bay Formation
206 were previously grouped together and called the 'Society Cliffs Formation' (Blackadar and Lemon, 1963).
207 The lower part of these carbonates also contains evaporitic facies, including laterally continuous massive
208 and laminated gypsum ($CaSO_4$) beds that appear to reflect precipitation in the water column in some
209 locations and small, decimeter-scale pods in other locations within the basin. This gypsum has $\delta^{34}S$ values
210 between +21.5 and 36.4‰ (Kah et al., 2004; Crockford et al., 2019).

212 The degree of connectivity between the Borden Basin and the global ocean is uncertain but likely varied
213 through time. The high availability of sulfate and some metals (Hodgskiss et al., 2020) argues for at least
214 an occasional marine connection (e.g., during deposition of the Iqqituq and Angmaat formations overlying
215 the Arctic Bay Formation). However, based on initial Os isotope values and REE+Y trends, some authors
216 have argued that the Arctic Bay Formation was deposited in a much more restricted setting such as an
217 alkaline lacustrine environment (Hahn et al., 2015; Gibson et al., 2019).

219 The redox structure of the Arctic Bay depositional environment is constrained by iron speciation and trace
220 metal abundance records in the context of global Mesoproterozoic redox evolution. Based on elevated total
221 S contents and enrichments in Mo, U, and V (Hodgskiss et al., 2020), the lower half of the Shale Valley
222 section appears to have been ferruginous and intermittently euxinic. In the Alpha River section, the highest
223 TOC contents are found between 580-780 m of stratigraphic height. These shales are also characterized by
224 relatively high degree of pyritization, although ratios of pyrite iron (Fe_{py}) to highly reactive iron (Fe_{HR}) are
225 below canonical thresholds for euxinia (~0.6 versus ~0.7). These Alpha River black shales are particularly
226 notable for containing 'excess' sulfur beyond that attributable to barite or pyrite, which, if associated with
227 organic matter, would imply remarkably high kerogen S:C ratios (Hodgskiss et al., 2020). Other parts of
228 both sections, however, indicate primarily ferruginous (anoxic, non-sulfidic) conditions. Carbonate-
229 associated iron (Fe_{carb}) is abundant and can comprise up to half of the highly reactive iron pool (Fe_{HR})
230 (Hodgskiss et al., 2020).

232 Although global productivity during the Mesoproterozoic is thought to have been relatively low due to
233 nutrient limitation under anoxic deep ocean conditions (Derry, 2015; reviewed in Lyons et al., 2021),
234 productivity in the Borden Basin may have been locally high due to a riverine or other influx of phosphate
235 (Laakso and Schrag, 2019). High TOC contents in the Arctic Bay Formation persist despite ca. 1 Gyr of
236 maturation and diagenesis. These sections have relatively low thermal overprints by Mesoproterozoic
237 standards, but they have experienced heating and pressurization, sufficient to reach the 'dry gas' window
238 (Ro% of 1.4) and expel most bitumens (Fustic et al., 2017). This process, referred to as 'cracking,' degrades

aliphatic monosulfide and disulfide bonds and, by Ro% ~1.5, generates thiophenic sulfur in artificial maturation and heating experiments (Sarret et al., 2002; Amrani et al., 2005; Kelemen et al., 2012). Cracking and bitumen generation reduce the total amount of organic S remaining in kerogen by as much as 6–7-fold (Amrani et al., 2005) and can cause aromatization and other rearrangements within the remaining sulfur-carbon backbone of the kerogen polymers (Rosenberg et al., 2017; Jin et al., 2021). Organic matter in Arctic Bay shales thus records a likely restricted marine environment with nonetheless large reservoirs of S, Mo, and trace metals, intermittently sulfidic and anoxic conditions (Hodgskiss et al., 2020), and elevated primary productivity near coasts, the preservation of which was modified by heating and maturation during diagenesis.

2.2 Sample Collection and Storage

Shale samples were collected from outcrops. To collect relatively 'fresh' samples, weathered surface material was broken off using a geological hammer, and samples were then hammered off the outcrop. Samples were stored in cloth sample bags so to allow moisture to escape and reduce weathering during transportation and storage, while also minimizing contamination. Shale samples were trimmed with a diamond saw to remove any remaining weathered portions. Samples were splits of the same powders analyzed in Hodgskiss et al. (2020).

2.3 Sequential Extractions and Kerogen Isolation

Bitumen and elemental sulfur were microwave-extracted (MARS-6, CEM) from 2-gram powdered rock samples twice in 20 mL of 9:1 dichloromethane:methanol (15 minutes at 70°C) at the University of California, Santa Barbara (UCSB). Solvent extracts were evaporated under N_2, visually inspected for S^0 crystals, and weighed. Remaining solids were then subjected to acid-volatile sulfide (AVS) and chromium-reducible sulfide (CRS) extractions (Canfield et al., 1986) at Stanford University, after which solids, extracts, and acid solutions were returned to UCSB. For both AVS and CRS extractions, sulfide gas was trapped in 5% zinc acetate solution, washed, oxidized to sulfate in 30% hydrogen peroxide, and quantified as dissolved sulfate by ion chromatography (Metrohm 930 IC / 889 with Metrosep A Supp 7 150 x 4.0 mm anion column) at UCSB. AVS was not detectable above process blanks and is not discussed further. CRS-derived sulfates were precipitated with excess $BaCl_2$, washed, dried, and weighed for S-isotope analysis as $BaSO_4$. Organic matter in CRS-extracted solids is considered 'kerogen' and was subdivided for elemental ratio, S-isotope, and X-ray absorption spectroscopy analyses. Carbon and sulfur contents of CRS-extracted sediments were measured via combustion on an Eltra CS-500 analyzer at the University of California Riverside (UCR). Both C wt% and S wt% were calibrated using Alpha Resources standard AR-4019 (C

272 wt% = 0.102, 1σ = 0.008 and S wt % = 0.100, 1σ = 0.005). During analysis, the measured precision (1σ)

273 of AR-4019 was 0.007 wt% for C and 0.004 wt% for S.

274

2.4 Sulfate precipitation

276 Inorganic sulfates were solubilized during the AVS extraction in anoxic, hot (60°C) 6N hydrochloric acid

277 and were separated from insoluble solids by centrifugation and decanting. Acid extracts were diluted

278 fivefold into ultrapure (milli-Q) water and combined with excess saturated $BaCl_2$ solution for ~12 hours to

279 precipitate sulfate as $BaSO_4$. Precipitates were centrifuged and washed 4x in ultra-pure water before

280 weighing and S-isotope analysis.

281

2.5 Pyrite triple-isotope analyses

283 Sulfur isotope analyses of pyrites were conducted in the McGill Stable Isotope Laboratory following

284 standard methods (Kunzmann et al., 2017). Samples were washed with ultra-pure water (milli-Q), dried

285 and crushed in a chrome-steel ringmill. Powdered samples (~0.2 –15 g depending on S content) were placed

286 into a vessel, flushed with $N_2(g)$, and subjected to CRS extraction as above (Canfield et al., 1986). The

287 $H_2S(g)$ generated was carried in an N_2 stream and bubbled into a 4% zinc acetate solution to convert $H_2S(g)$

288 to ZnS(s). The ZnS(s) was converted to Ag_2S through the addition of 1 mL of 1 M $AgNO_3$. Samples were

289 filtered and then dried in an oven at ~80˚C. For sulfur isotope analysis, 3 mg of Ag_2S were weighed into

290 aluminum foil packets which were then placed into nickel bombs. Samples were reacted under

291 a fluorine gas (F_2) atmosphere at 250 °C for 12 h to convert $Ag_2S(s)$ to sulfur hexafluoride gas ($SF_6[g]$). The

292 resulting SF_6 gas was then purified progressively along a vacuum line through multiple cold-traps under

293 vacuum, followed by gas chromatography. Purified samples were analyzed in dual inlet mode on a Thermo

294 MAT-253. Results were measured against international standard reference material IAEA-S1 ($\delta^{34}S$ = –

295 0.3‰ and $\Delta^{33}S$ = –0.061). Estimated maximum errors (1σ) on measurements and the entire analytical

296 procedure are 0.1‰ for $\delta^{34}S$ and 0.01‰ for $\Delta^{33}S$.

297

2.6 Multi-phase sulfur-isotope analyses

299 Sulfur isotope analyses for CRS extracts (as $BaSO_4$), sulfates (as $BaSO_4$), and post-CRS residuals (kerogen)

300 were performed at UCR in the Lyons Biogeochemistry Laboratory with a Thermo Scientific Delta V Plus

301 continuous-flow stable isotope ratio mass spectrometer (IRMS). Sulfur from all sample types was converted

302 to SO_2 and separated via gas chromatography on a Costech ECS 4010, with gas flow to the IRMS being

303 controlled by a Thermo Scientific ConFlo III open split interface. Kerogens were bracketed by the

304 international measurement standards IAEA-S1 (–0.30‰), IAEA-S2 (22.67‰), and IAEA-S3 (–32.55‰);

305 $BaSO_4$ samples were bracketed by IAEA-SO5 (0.49‰), IAEA-SO6 (–34.05‰), and NBS-127 (21.1‰).

306 Precision of standards (1σ) was 0.9‰ or better for all kerogen analyses and 0.4‰ or better for all BaSO$_4$

307 analyses.

308

309 **2.7 X-ray absorption spectroscopy**

310 The redox speciation and bonding environment of sulfur in whole and CRS-extracted sediments were

311 analyzed at beam line 14-3 at the Stanford Synchrotron Radiation Lightsourse (SSRL). Powdered samples

312 were mounted on St Gobain M60 S-free polyester tape and covered in 5-µm-thick SPEX 3520

313 polypropylene XRF film. XAS spectra were collected from 2460 to 2540 eV (Fig. S1), as calibrated to the

314 thiol pre-edge peak of thiosulfate at 2472.02 eV. The X-ray beam was trimmed to a size of 500 x 500 µm

315 at a flux of ~8 x 10^{10} photons per second. Beam line 14–3 is equipped with a Si(111) (Φ = 90) double crystal

316 monochromator, and the S Kα fluorescence line is measured with a Si Vortex Si drift detector (Hitachi)

317 using Xspress3 pulse processing electronics (Quantum Detectors). Sulfur XAS spectra were processed in

318 the SIXPACK (Webb, 2005) software package using a K-edge E^0 of 2473 and pre-edge and post-edge linear

319 normalization ranges of –20 to –7 and 35 to 70 eV, respectively. Spectra were fit to a set of eight organic

320 and six inorganic standard spectra (Fig. S2), which are presented grouped by major functional type:

321 aromatics (dibenzothiophene, thianthrene), alkyl sulfides (methionine), alkyl disulfides (phenylene

322 disulfide, glutathione disulfide), sulfoxides (methionine sulfoxide), sulfonates (cysteic acid), organic sulfate

323 esters, elemental S, pyrite, iron monosulfides (mackinawite, pyrrhotite), and sulfates (sodium sulfate,
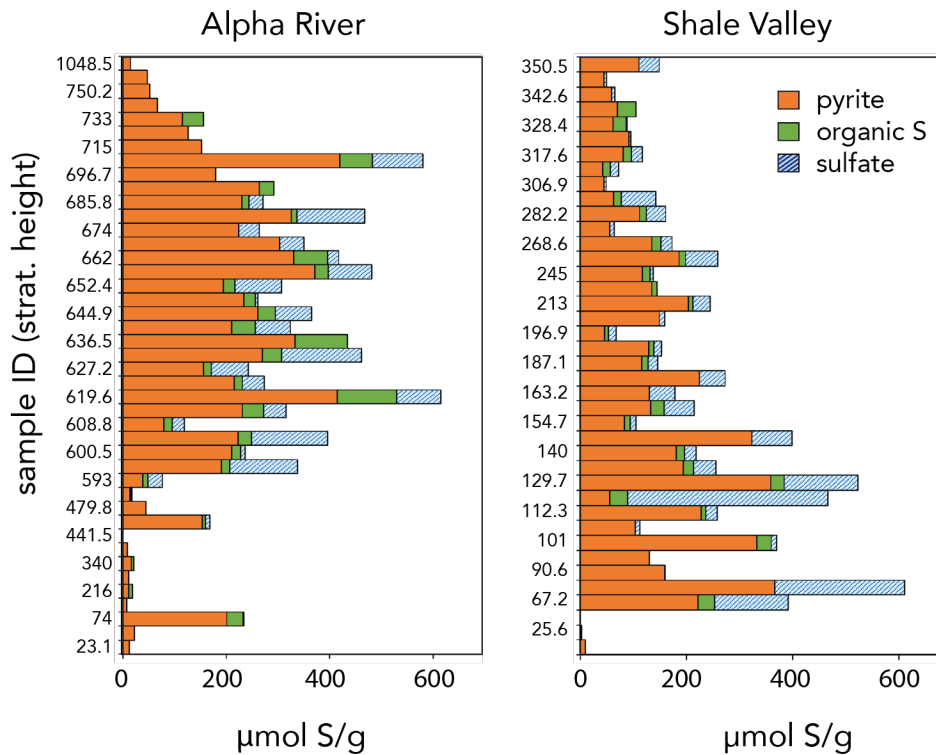
324 gypsum).

325

326

327 **3. RESULTS**

328

329 **3.1 Concentrations of sulfur phases**

Fig. 2 - Concentrations of pyrite, organic S, and inorganic sulfate in Arctic Bay Formation black shales. Data are from sequential chemical extractions. Samples are arranged by stratigraphic height order; every-other sample ID is shown for legibility (Table S1). Total sulfur is primarily pyrite, although a few samples contain more acid-soluble sulfate than pyrite. Total sulfur in both sections includes an average of approximately 16% acid-soluble sulfate and 11% organic S.

Alpha River samples contain between 7 and 420 μmol S_{py}/g (0.04 to 2.5 wt% FeS_2), and Shale Valley samples contain between 2 and 366 μmol S_{py}/g (0.01 to 2.2 wt% FeS_2). Pyrite concentrations (Figure 2 and Table S1) are relatively high in the TOC-rich black shales from Alpha River and in some black shales from the lower part of the Shale Valley section. Pyrite concentrations reported here represent corrected versions of the data reported in Hodgskiss et al. (2020), which contained a calculation error. After pyrite, the second most abundant sulfur phase is acid-soluble sulfate, defined as sulfur that was solubilized in strong acid (6N HCl, 60°C, 2 hrs) and trapped as sulfate (with Ba^{2+}). Inorganic sulfate, carbonate-associated sulfate (CAS), and sulfate-rich minerals like gypsum and phosphates are also trapped as part of this acid-soluble pool, as are some organic sulfate esters. Visible $BaSO_4$ precipitates formed in 58 of the 82 total sample extracts and represented concentrations of up to 155 μmol S_{so4}/g in Alpha River and up to 377 μmol S_{so4}/g in Shale Valley. Organic (kerogen) sulfur concentrations ranged from < 0.2 to 115 μmol S_{org}/g in Alpha River and from 0.4 to 91.4 μmol S_{org}/g at Shale Valley. Organic solvent extractions did not yield detectable bitumen

or elemental S. Published total S concentrations from splits of these same samples (Hodgskiss et al., 2020) are an average of 22% higher than the sum of phases recovered in the current study. Missing S in this mass balance could have been present as acid-soluble, non-Ba-reactive organic S or could have been lost during the manual transfer of $BaSO_4$ powders for weighing and/or during CRS recovery (typically ~93-99% efficient; Canfield et al., 1986). Sulfur was not detected in the acid-volatile (AVS) or organic solvent-extracted (lipid/S^0) pools.

Consistent with published datasets (Table S1), TOC concentrations in Alpha River averaged 4.1 mmol C_{org}/g (5.0 wt% TOC) and ranged from 0.5 to 11.3 mmol C_{org}/g (0.6 to 13.6 wt% TOC). In Shale Valley, TOC concentrations averaged 5.7 wt% and ranged from 0.7 to 12.3 wt%. The molar sulfur-to-carbon (S:C) ratios of this organic matter average 0.8 mol% (S:C = 0.8 : 100 mol/mol) in Alpha River and 0.6 mol% in Shale Valley. S:C ratios of ≥2.0 mol% were found in just four samples from Alpha River and two samples from Shale Valley; the absence of pyrite in these kerogens was confirmed by XAS.

3.2 X-ray absorption spectroscopy
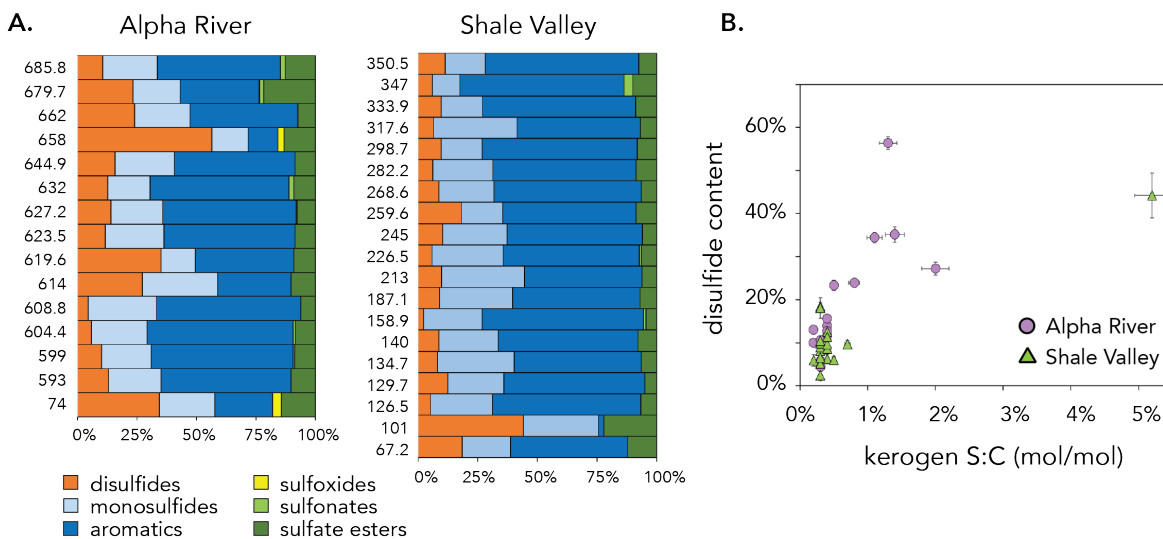
Fig. 3 – Speciation of organic S in Arctic Bay kerogens. A: Organic sulfur species are ordered from most reduced (left) to most oxidized (right). Fitting errors on each component are typically 1-2% (Table S1). B: Relationships between kerogen S:C ratio and disulfide content for Alpha River (circles) and Shale Valley (triangles), showing elevated disulfide contents in S-rich samples. Only good-quality fits are shown (chi-squared values ≤ 30); see Table S1 for fit quality parameters and extended dataset.

13

373   X-ray absorption spectroscopy (XAS) was conducted at SSRL to identify the speciation and redox state of

374   organic and total sulfur in shale samples (Figure 3 and Table S1). Kerogen sulfur (S_{org}) spectra were

375   collected for all rock powders containing measurable S. A subset of 16 samples was also measured by XAS

376   prior to sequential extractions to evaluate the distribution of sulfur phases before chemical treatments and

377   to assess the completeness of our mass balance. Consistent with Figure 2, whole rock sulfur spectra contain

378   variable proportions of pyrite, sulfate, and reduced organic sulfur as the major phases present (Table S1,

379   Fig. S1).

380

381   Organic sulfur in kerogen is on average 90.6% 'reduced'; the remaining (oxidized) organic S best resembles

382   sulfate esters. A primary XAS feature at 2474.0 eV indicates aromatic organic sulfur moieties, similar to

383   dibenzothiophene but lacking its secondary structure at 2479 eV (Fig S1). Due to the energy overlap among

384   specific organic sulfur species in the 2473 – 2474 eV range and the signal-to-noise ratio of these spectra,

385   there is high uncertainty related to the relative abundances of aromatic versus monosulfide sulfur; in many

386   cases, fit quality parameters are only slightly less favorable when calculated with no organic monosulfide

387   component. In contrast, we can clearly distinguish between this primarily aromatic material and a feature

388   near 2472.4 eV that represents an organic S form with a lower effective 'oxidation index,' which is best fit

389   as disulfide (Vairavamurthy, 1998). Samples from Alpha River generally contain a larger proportion of

390   disulfide organic S (4 – 35%, averaging 16.5%) than those from Shale Valley (5 – 19%, averaging 10%).

391   The highest proportions of organic disulfides are present in samples with elevated S:C ratios (Fig. 3b), and

392   this trend continues with lower precision in lower-quality fits (Table S1).

393

394   **3.3 Sulfur-isotope compositions**
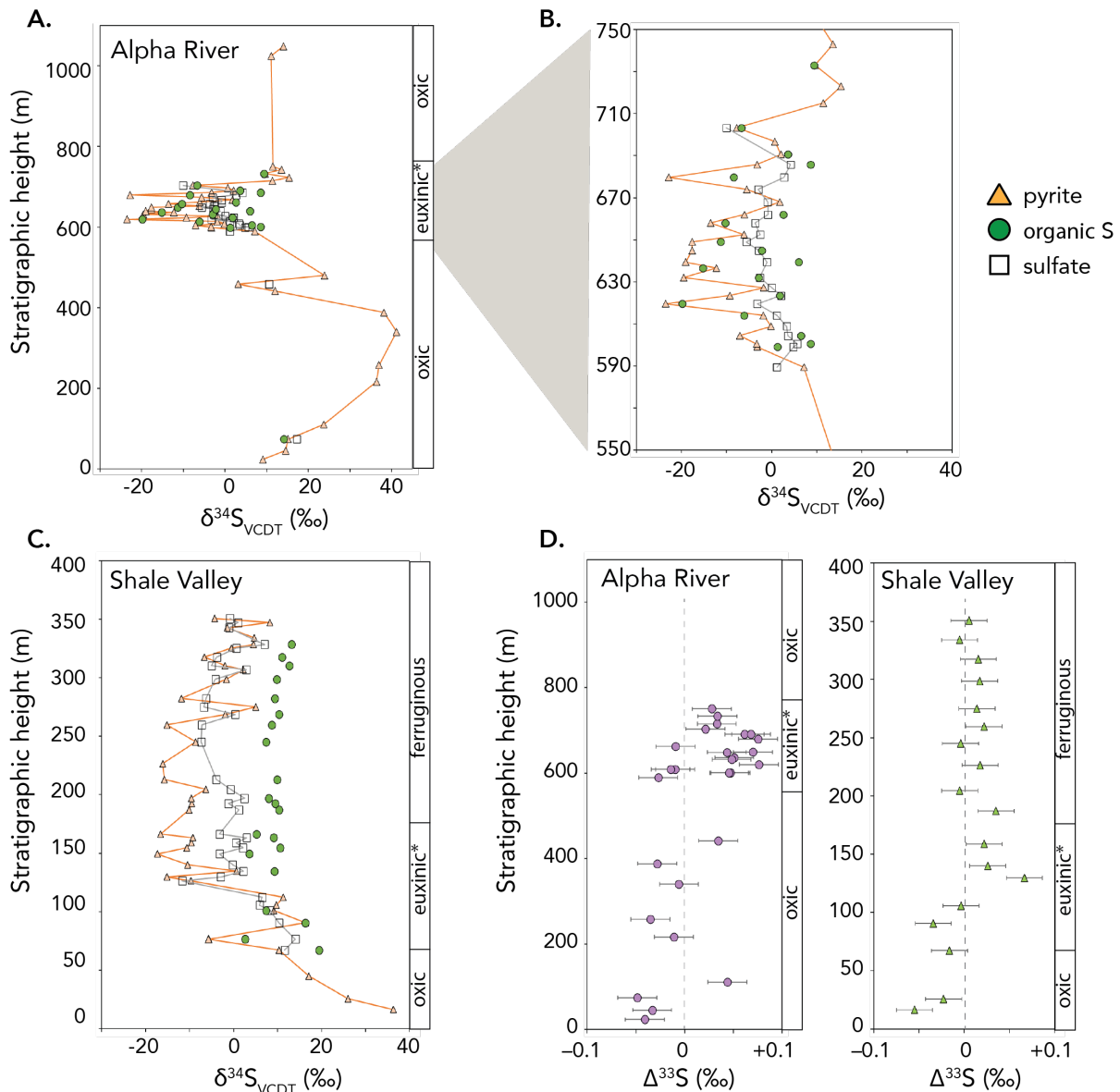
Fig. 4 - Stratigraphic profiles of sulfur-isotope compositions. Panels A, B, and C show $\delta^{34}S$ values for pyrite (triangles), organic S (circles), and acid-soluble sulfate (open squares); panel B replicates data in (A) in higher resolution. Uncertainties are smaller than symbols (±0.4‰ for pyrite and sulfate, ±0.9‰ for organics). Panel D shows the minor-isotope composition ($\Delta^{33}S$) of pyrite in both sections. Bars along the right-hand side of profiles show inferred local redox conditions, where 'euxinic*' indicates ambiguous and/or intermittent euxinic conditions (Hodgskiss et al., 2020).

Sulfur-isotope compositions ($\delta^{34}S$ values) were measured for three coexisting sulfur phases in Arctic Bay shales: pyrite, kerogen, and acid-soluble sulfate. Pyrite $\delta^{34}S$ values range from –23.5‰ to +41.2‰ and

show coherent shifts across the sections. In Shale Valley, pyrite is strongly ^{34}S-enriched in the lowest part of the section and becomes gradually more depleted (–10‰ ± 10‰) by 125 m stratigraphic height. Pyrite δ^{34}S values return to slightly higher values in the upper part of the section (275 –350 m) but never exceed +8.2‰. In the Alpha River section, large, coherent δ^{34}S shifts and strongly ^{34}S-enriched values characterize the lower, less-TOC-rich part of the section (≤550 m), with a maximum δ^{34}S value of +41.2‰ at 340 m. In contrast, all pyrite δ^{34}S values between 593 and 686 m are moderately ^{34}S-depleted, with values between –23.5 and +1.8‰ (Fig. 4). Pyrite in the upper Alpha River section (>710 m) has an intermediate S-isotope composition ranging from +9.6 to +15.4‰.

The isotopic composition of organic sulfur ranges from –19.8 to +14.1‰ at Alpha River and from +9.7 to +19.4‰ at Shale Valley (Fig. 4 and Table S1). Organic S at Alpha River is generally more ^{34}S-depleted than at Shale Valley, and the average δ^{34}S difference between pyrite and organic S (ε_{PK}) is smaller at Alpha River (6.3‰) than at Shale Valley (15.0‰). At the same time, maximum ε_{PK} values for individual samples are similar at both sites (25.0‰ and 25.6‰, respectively; Fig. 3, Table S1). Organic S is slightly more ^{34}S-depleted than pyrite, by as much as 4.3‰, in 5 of 24 samples at Alpha River and 2 of 21 samples at Shale Valley. Samples with this relatively atypical, reversed S-isotope pattern (Vairavamurthy et al., 1995) are scattered throughout both sections and associated with pyrites that are generally ^{34}S-enriched relative to surrounding layers, consistent with the addition of ^{34}S-enriched, later-stage pyrite.

Sulfate δ^{34}S values fall within the same range as organic sulfur and pyrite throughout the sections, ranging from –11.7 to +17.2‰ and averaging +0.5‰. Sulfate δ^{34}S values show a close relationship with pyrite δ^{34}S in some parts of the sections. In the upper part (>250 m) in the Shale Valley section, for example, both parameters vary in concert and remain within 5‰ of each other. Such isotopic agreement often points to pyrite oxidation as the source of (secondary) sulfate (see details in the Discussion below). Other parts of the sections preserve larger offsets between the two pools – for example, at Shale Valley between 130 and 250 m – where sulfate δ^{34}S values are on average 10.4‰ (range 5.9 to 14.8‰) more ^{34}S-enriched than coexisting pyrite. Sulfate δ^{34}S values show less variability than pyrite δ^{34}S values through the Alpha River shales between 590 and 710 m.

The minor-isotope (Δ^{33}S) composition of pyrite ranges from –0.05‰ to +0.08‰ (Fig. 3d). Many Shale Valley values are near zero (average +0.01‰). Minimum Δ^{33}S values (-0.05‰) are found in the lower, apparently oxic portions of both sections, alongside ^{34}S-enriched pyrites. Pyrite Δ^{33}S values are significantly greater than zero (average +0.04‰) in many samples deposited under apparently intermittently sulfidic

439 conditions, including many samples from Alpha River between 590-690 m and one sample from Shale
440 Valley (129.7 m, +0.07‰).

441

442 **4. DISCUSSION**

443

444 **4.1 Sulfate sources and implications for iron speciation**

445 Sulfate in sedimentary rocks is often derived from seawater sulfate, whether it is present as an evaporative
446 salt mineral like gypsum ($CaSO_4$) or incorporated within the crystal lattice of a carbonate mineral (i.e.,
447 carbonate-associated sulfate, or CAS). Seawater-derived sulfates in both forms are well known from the
448 Iqquittuq and Angmaat formations, overlying the Arctic Bay Formation, where the $\delta^{34}S$ of evaporative
449 gypsum layers is ~+22‰ (Kah et al., 2001, 2004; Johnston et al., 2005) (Fig. 1). These sulfate S-isotope
450 compositions serve as our best estimate for basin seawater sulfate $\delta^{34}S$ during Arctic Bay deposition. Unlike
451 CAS and gypsum minerals in overlying strata, acid-soluble sulfates from Arctic Bay Formation shales have
452 distinctively ^{34}S-depleted compositions that are similar to coexisting pyrite and organic S, which indicates
453 that the primary source of sulfate to Arctic Bay rocks is the oxidation of pyrite and/or organic sulfur.

454

455 Pyrite oxidation during the weathering of shales is well known and can extend tens of meters below the
456 outcrop surface (Gu et al., 2020). Pyrite oxidation can also occur during sample handling. During pyrite
457 oxidation by O_2, sulfur is oxidized to sulfate while ferrous iron is oxidized to Fe^{3+}. In shales that contain
458 sufficient carbonates to buffer against acid accumulation and related Fe^{3+} solubility, the ferric iron (Fe^{3+})
459 produced by pyrite oxidation is generally retained as oxide mineral phases (Pye and Miller, 1990; Brantley
460 et al., 2013; Mahoney et al., 2019). Arctic Bay shales contain abundant carbonates (averaging 39 wt%), so
461 they were presumably pH-buffered during pyrite oxidation and are unlikely to have experienced substantial
462 iron loss. This assumption is important for our understanding of Fe_{HR} concentrations (see below).

463

464 Unlike iron, the sulfate produced during pyrite oxidation can either be mobile in oxidizing fluids or retained
465 as gypsum ($CaSO_4$), in phosphates, or as jarosite ($KFe_3(SO_4)_2(OH)_6$) (Chandra and Gerson, 2010). Elevated
466 concentrations of acid-soluble sulfate were present in nearly all samples with moderate-to-high pyrite
467 concentrations (Fig. 2), yielding a rough positive association between pyrite and sulfate concentrations (Fig.
468 S3). The close correspondence between pyrite and sulfate $\delta^{34}S$ values in the upper part of the Shale Valley
469 section indicates that acid-soluble sulfates derived primarily from local S_{py} oxidation (Fig. 4). In the
470 densely-sampled, TOC-rich Alpha River shales between 600-700 m, however, sulfate $\delta^{34}S$ values are less
471 variable and an average of 9.7‰ higher than pyrite $\delta^{34}S$ values. Mixing with ^{34}S-enriched sulfate from
472 evaporites is unlikely to explain this S-isotope difference because we lack lithological evidence for

473   subaerial exposure or related evaporite deposition in these sections (see Fig. 1 for regional evaporite

474   locations). Potential contributions from CAS are also small: if CAS were present at a concentration of 100

475   ppm in carbonate in these shales (Kah et al., 2004), it would account for an average of 0.7% of observed

476   acid-soluble sulfate concentrations (see Table S1). Instead, the differences between pyrite and sulfate δ^{34}S

477   values in TOC-rich Alpha River shales (600-700 m) could reflect contributions to the acid-soluble sulfate

478   pool from the local oxidation of abiogenic organic sulfur (Petsch et al., 2000) and/or sulfate mobilized from

479   pyrite oxidation in under- and overlying layers (Fig. 4).

480

481   Both pyrite (FeS_2) and its oxidation products like $Fe(OH)_3$ are considered 'highly reactive iron' or Fe_{HR}

482   (Canfield, 1989). If the iron oxidized during pyrite oxidation is retained locally (<mm-scale), this

483   transformation has no effect on the Fe_{HR}/Fe_T ratio used to classify environments as oxic or anoxic (Mahoney

484   et al., 2019). However, pyrite oxidation can decrease the ratio Fe_{Py}/Fe_{HR}, which is used to determine whether

485   environments were sulfidic (Poulton and Canfield, 2005; Raiswell et al., 2018). If we assume that total acid-

486   soluble sulfates represent solely the products of local pyrite oxidation and that no Fe_{HR} was diagenetically

487   transferred to the unreactive pool, we can estimate original Fe_{Py}/Fe_{HR} ratios prior to pyrite oxidation (Fig.

488   S4). These values are minima if sulfate loss exceeded sulfate gain, although the scale of sulfate mobilization

489   is poorly constrained. Still, corrected values should more closely resemble initial ratios for Fe_{Py}/Fe_{HR} than

490   uncorrected values. Reconstructed Fe_{Py}/Fe_{HR} ratios (Fig. S4) are slightly higher than those originally

491   reported in Hodgskiss et al. (2020), but maximum Fe_{Py}/Fe_{HR} ratios of 0.66 in both sections still fall below

492   the canonical euxinic threshold (Poulton and Canfield, 2005).

493

494   **4.2 Pyrite isotope patterns and local redox conditions**

495   The S-isotope composition of pyrite is a complex function of overlapping biogeochemical and

496   sedimentological processes within and overlying the sediment column. A principal driver of S-isotope

497   patterns in the environment is the strong fractionation imparted by sulfate reducing microorganisms, which

498   preferentially use lighter S-isotopes, producing ^{34}S-depleted sulfide and driving residual sulfate toward

499   higher δ^{34}S values. Variations in the fractionation factor associated with microbial sulfate reduction (MSR)

500   can thus impact the δ^{34}S values of sulfide and its products. For example, apparent fractionation factors

501   during MSR can decrease in response to higher-quality OM sources and correspondingly elevated cell-

502   specific metabolic rates (Chambers et al., 1975; Leavitt et al., 2013). Strongly ^{34}S-depleted pyrite (<-20‰)

503   is typically formed in environments that host microbial sulfate reduction in the water column or very

504   shallow sediments, where sulfate is replete due to the large seawater reservoir or efficient diffusive

505   exchange with the immediately overlying water column, respectively (Lyons, 1997; C. Li et al., 2010;

506   Pasquier et al., 2017; Raven et al., 2018; Houghton et al., 2022). As the rate of sulfate supply decreases

507   relative to the rates of sulfate reduction and pyrite formation, for example in more deeply buried sediments,

508   environments tend to record smaller differences between the δ^{34}S values of seawater sulfate and

509   sedimentary pyrite (Zaback et al., 1993; Fike et al., 2015; Liu et al., 2021). Microbial sulfate reduction in

510   OM-rich sediments thus generates profiles approximating Rayleigh distillation, with declining pore water

511   sulfate concentrations and increasing sulfate δ^{34}S values with depth (Jorgensen, 1979). Not all ^{34}S-enriched

512   pyrites form in deep sediments, however. Strongly ^{34}S-enriched sedimentary pyrites, including some with

513   δ^{34}S values exceeding seawater sulfate, are found in modern, shallow-water sediments that experience

514   episodic deposition, oxidative reworking, and other non-steady-state processes, especially in the presence

515   of reactive iron minerals (Aller et al., 2010). Freshwater lakes or restricted marine basins with low sulfate

516   concentrations can also develop isotopically distinctive sulfate reservoirs, depending on the relative rates

517   of microbial sulfate reduction versus sulfate replenishment (Lyons et al., 2000). During heating and

518   catagenesis, organic S breakdown in the presence of iron (Amrani et al., 2005; Siedenberg et al., 2018; see

519   below) can also contribute to pyrite δ^{34}S values. Pyrite has been shown to reductively degrade in higher

520   stages of thermal maturation in experimental settings, especially in the presence of H_2 and water, but natural

521   systems like the Arctic Bay shales are unlikely to result in a pyrite decomposition regime (Rosenberg et al.,

522   2017).

523

524
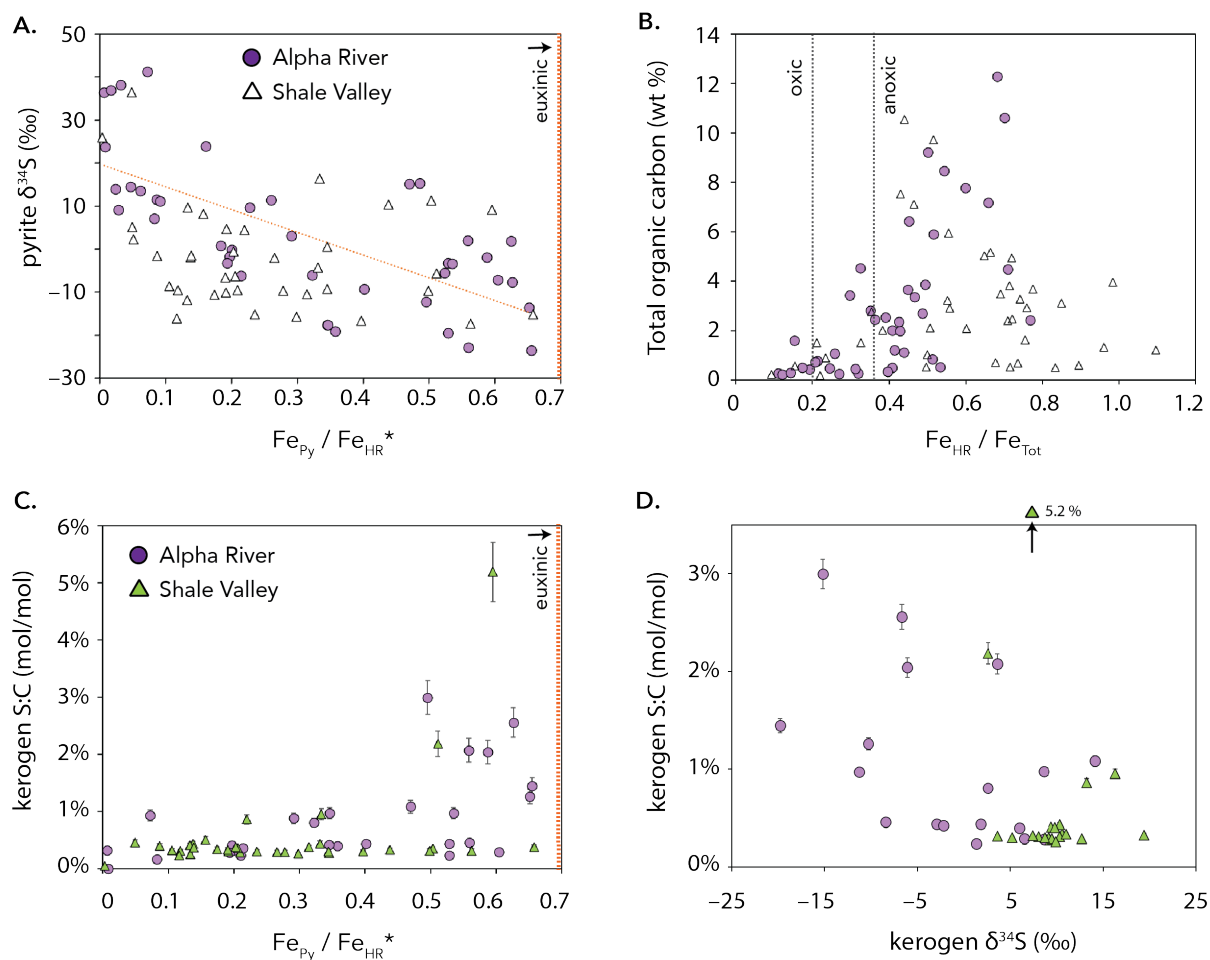
Fig. 5 – Redox state / organic matter relationships. (a) Relationship between the redox indicator for ferruginous-to-sulfidic conditions, Fe_{Py}/Fe_{HR}, and the S-isotope composition of pyrite. Iron ratios are reconstructed (*) to account for pyrite oxidation based on Hodgskiss et al. (2020), as shown in Figure S4. The regression line ($R^2 = 0.38$) applies only to data from Alpha River (purple circles). (b) Relationship between the redox indicator for oxic-to-anoxic conditions, Fe_{HR}/Fe_T (Hodgskiss et al., 2020), and total organic carbon (TOC) concentrations, showing canonical thresholds for oxic, anoxic, and ambiguous redox conditions (Poulton and Canfield, 2005). (c) Relationship between Fe_{Py}/Fe_{HR} and the S:C ratio of kerogen. (d) Relationship between the S-isotope composition and S:C ratio of kerogen; note the adjusted y-axis relative to (c).

Pyrite is relatively [34]S-enriched at the bottom of both Arctic Bay sections (Fig. 3), with some pyrite δ^{34}S values exceeding estimates for basin seawater sulfate (Kah et al., 2001; Crockford et al., 2019). Throughout this lower interval, trace metals, iron speciation, and lithologies are consistent with deposition under oxic water column conditions (Hodgskiss et al., 2020). Therefore, relatively [34]S-enriched pyrite could indicate

539   that the sulfidic front and thus the location of pyrite formation were relatively deep in the sediments.

540   Alternatively, and especially at the shallower-water Alpha River site, ^{34}S-enriched pyrite could also stem

541   from episodic, oxidative reworking and rapid pyritization in near-surface sediments. In either case, ^{34}S-

542   enriched pyrite compositions support the interpretation that the overlying water column was not sulfidic

543   during the deposition of stratigraphically lower, relatively TOC-lean Arctic Bay Formation shales.

544

545   Pyrite is relatively ^{34}S-depleted in both sections during intervals characterized by more TOC-rich black

546   shales (600-700 m at Alpha River and above 125 m at Shale Valley). More ^{34}S-depleted pyrite likely reflects

547   a shallowing of the redox interface into very shallow sediments or the water column associated with more

548   reducing local environmental conditions. This interpretation is consistent with reported depletions in barium

549   concentrations across these intervals compared with surrounding strata (Hodgskiss et al., 2020). At Alpha

550   River, ^{34}S-depleted pyrites are weakly correlated with reconstructed iron speciation indicators for more

551   reducing (possibly sulfidic) conditions (Figure 5a). Trace metals and iron speciation at Shale Valley

552   (Hodgskiss et al., 2020) also broadly suggest an association between more ferruginous to possibly sulfidic

553   conditions and ^{34}S-depleted pyrite. Overall, pyrite S isotopes appear to record a shift in the location of sulfur

554   cycling and pyrite formation between deeper (and/or reworked) sediments during oxygenated periods and

555   shallower sediments (and/or the water column) during more reducing periods.

556

557   Minor sulfur isotope ratios (Δ^{33}S) can help distinguish among processes with slightly different mass

558   fractionation relationships, for example microbial sulfate reduction ($\lambda \sim 0.515$) and sulfur

559   disproportionation (Johnston et al., 2005; Kunzmann et al., 2017). The latter has a stronger relative

560   preference for ^{33}S and generates sulfate with δ^{33}S values that are higher than those expected in an

561   environment hosting only microbial sulfate reduction (Bradley et al., 2016). Rocks overlying the Arctic

562   Bay Formation shales (Angmaat Formation) contain carbonate-associated sulfate that is slightly ^{34}S-

563   enriched relative to near-coeval gypsum layers and has a resolvable Δ^{33}S enrichment (up to 0.07 ±0.02‰)

564   that Johnston et al. (2005) interpreted as requiring sulfur disproportionation. However, the subsequent

565   recognition of the expanded range of possible sulfur isotope fractionations ($^{34}\varepsilon_{MSR}$) at low cell-specific

566   sulfate reduction rates (Sim et al., 2011) leaves the role of disproportionators ambiguous. In the Arctic Bay

567   Formation, pyrite Δ^{33}S compositions are systematically positive in intervals interpreted as intermittently

568   sulfidic, where pyrite is generally abundant and ^{34}S-depleted (Fig. 4). This pattern is widely observed as a

569   result of microbial sulfate reduction in modern sulfate-replete environments (Canfield et al., 2010; Zerkle

570   et al., 2010; X. Li et al., 2010) and is consistent with previous findings exploring Proterozoic sulfur cycling

571   (Kunzmann et al., 2017). The appearance of relatively ^{33}S-enriched, ^{34}S-depleted pyrite in the Arctic Bay

572   Formation supports the presence of sulfate concentrations >1 mM (Harrison and Thode, 1958; Johnston,

573 2005), in agreement with estimates based on rates of sulfate isotope variation in overlying strata (up to 4.5
574 mM; Kah et al., 2004). In contrast, small and consistent fractionations between carbonate–associated sulfate
575 and pyrite in earlier Mesoproterozoic sections have been interpreted to reflect sulfate concentrations <<1
576 mM (~1.7 – 1.4 Ga; Luo et al., 2015). To the extent that the Borden Basin records global marine chemistry,
577 it suggests that marine sulfate concentrations may have significantly increased during the Mesoproterozoic,
578 between ~1.4 and ~1.05 Ga, or that factors other than low sulfate concentrations led to the small apparent
579 fractionations in the early Mesoproterozoic.
580
581 **4.3 Organic sulfur formation and local redox conditions**
582 Organic sulfur in Alpha River shales is isotopically similar to coexisting pyrite and is strongly [34]S-depleted
583 relative to estimates for late Mesoproterozoic seawater, so it primarily represents the products of abiotic
584 sulfurization in the water column or shallow sediments. OM sulfurization therefore occurred at
585 approximately the same time as pyritization at the shallower-water, more shelf-like site. In contrast, organic
586 S is consistently more [34]S-enriched at Shale Valley, suggesting later diagenetic sulfurization in the deeper
587 basin.
588
589 Overall, these paired $\delta^{34}S_{py}$ and $\delta^{34}S_{ker}$ values for Arctic Bay shales overlap with the broad-scale patterns
590 observed in Phanerozoic O_2-limited environments (Vairavamurthy et al., 1995; Raven et al., 2019) and
591 provide the first isotopic records of syngenetic-to-early-diagenetic OM sulfurization (sulfurization in the
592 water column or shallow sediments) in the Proterozoic. A handful of paired pyrite and organic S data have
593 been published for shales and dolostones from significantly younger (Neoproterozoic; 850-500 Ma)
594 sections, but these samples are strongly [34]S-enriched, with S_{org} values between 8.5 and 50.6‰, and likely
595 reflect relatively later diagenetic formation in diffusively restricted sediments during atypical conditions
596 linked to the global recovery from a Snowball Earth (Gorjan et al., 2000; Cai et al., 2022). Going further
597 back in Earth history, OM sulfurization was also identified in one study of an Archaean microbial mat.
598 There, organic S was isotopically similar to pyrite, with $\delta^{34}S$ values sometimes less than –15‰, suggesting
599 early diagenetic sulfurization (Bontognali et al., 2012). Arctic Bay Formation kerogens thus help fill a more
600 than two-billion-year gap in our record of organic S across Earth history. As the first example of syngenetic-
601 to-early-diagenetic sulfurization of kerogens in an anoxic Proterozoic basin, they confirm that sulfur in
602 Proterozoic TOC-rich shales may represent the products of OM sulfurization reactions in the water column
603 or shallow sediments.
604
605 Elemental ratios of sulfur and carbon can complement isotopic evidence for OM sulfurization. Sulfurization
606 of highly functionalized organic matter can increase the sulfur content of kerogen relative to primary algal

607 and/or bacterial biomass, which has an initial S:C ratio near ~1 mol% (S:C = 1:100 mol/mol; Matrai and

608 Eppley, 1989; Chen et al., 1996). Kerogen S:C ratios therefore represent a rough indicator of sulfurization

609 intensity, at least for immature samples. Maturation and catagenesis cause the preferential loss of organic

610 S relative to C and will lower kerogen S:C ratios. Catagenesis of the Arctic Bay Formation shales exceeded

611 the oil and dry gas windows (Ro% = 1.4, see Site Description), so we expect that significant amounts of

612 organic sulfur, especially aliphatic sulfides and disulfides, have been preferentially lost and that measured

613 S:C ratios are lower than original S:C ratios by a factor of as much as 6–7 (Amrani et al., 2005; Kelemen

614 et al., 2012). However, sulfide loss from kerogen during heating appears to be unidirectional, and

615 catagenesis does not cause the incorporation of pyrite sulfur into kerogens (Kelemen et al., 2012). In this

616 context, most Arctic Bay Formation kerogen S:C ratios are low (generally less than 1 mol%), in contrast to

617 prior suggestions that these ratios might exceed several tens of percent (Hodgskiss et al., 2020). However,

618 one sample from Shale Valley has an S:C ratio of 5.2 mol%, and five others have S:C ratios between 2 and

619 3 mol%. These S:C ratios resemble kerogen S:C ratios from modern and Phanerozoic anoxic and sulfidic

620 basins (Raven et al., 2019) and indicate that the OM available for sulfurization contained a substantial

621 concentration of sulfurizable functional groups. Therefore, it appears that predominantly microbial

622 Mesoproterozoic biomass has the potential to sulfurize to a roughly comparable extent as its Phanerozoic

623 equivalent.

624

625 Despite organic S loss during catagenesis, Arctic Bay Formation shales also appear to preserve some

626 relationships between S:C ratios, S-isotope compositions, and organic S speciation (by XAS). Unlike S:C

627 ratios, the bulk S-isotope composition of kerogen is unlikely to change substantially during breakdown and

628 S-loss, as substantial isotopic changes were not observed in oils or kerogens during heating in semi-open-

629 system kerogen maturation experiments (Amrani et al., 2005; Rosenberg et al., 2017). Kerogen S:C ratios

630 only exceed 2 mol% in samples with reconstructed Fe_{Py}/Fe_{HR} ratios above 0.5 (Fig. 5c), approaching but

631 not exceeding the canonical threshold used to infer sulfidic conditions in the water column. Higher S:C

632 ratios are also associated with more [34]S-depleted kerogens (Fig. 5d), a pattern that may reflect early

633 sulfurization of relatively fresh, functionalized OM (Raven et al., 2018). Alpha River kerogens with high

634 S:C ratios also contain relatively large proportions of apparent organic disulfides (Fig. 3), which are

635 common OM sulfurization products (Kohnen et al., 1991; Amrani and Aizenshtat, 2004; Raven et al.,

636 2021b). Although these trends lack the clarity sometimes preserved in Phanerozoic sections, they

637 consistently point toward relatively extensive OM sulfurization in environments with generally ferruginous

638 to sulfidic (as opposed to oxic) water column conditions, most notably at the shallower Alpha River site.

639

640   In a marine system with a water column characterized as ferruginous based on trace metals or other proxies,

641   OM sulfurization in the water column will be limited by low sulfide availability. Sulfurization in these

642   systems therefore most likely occurred within restricted zones that facilitate the drawdown of reactive iron,

643   including shallow sediments, sulfidic wedges, or sinking marine particles, in analogy to anoxic sub-

644   environments in the modern predominantly oxygenated ocean. Although ferruginous conditions are not

645   intrinsically associated with a specific iron concentration, dissolved Fe^{2+} concentrations in the water column

646   must be sufficient to quantitatively titrate out sulfide as iron sulfide solids at interfaces with sulfidic

647   conditions and therefore may have been at micromolar levels (Scholz, 2018; van de Velde et al., 2020). If

648   anoxic, Fe^{2+}–rich water upwells into a shallower, sulfidic water mass, it is likely to cause extensive iron

649   sulfide formation at the iron-sulfide redox interface. In this scenario, extensive iron sulfide formation in the

650   water column might therefore have pushed pyrite formation to outcompete OM for sulfide, functionally

651   disfavoring early OM sulfurization (Shawar et al., 2018; Hartgers et al., 1997). This effect may contribute

652   to the relatively large $\delta^{34}S$ difference between pyrite and organic S throughout the ferruginous interval in

653   Shale Valley, where more [34]S-depleted pyrite suggests a syngenetic source, while relatively [34]S-enriched

654   organic S is consistent with later organic S formation in more diffusively-limited, sulfidic sediments.

655

656   Alternatively, relatively [34]S-enriched organic S in Shale Valley kerogen could reflect mixing with a

657   substantial amount of primary biogenic material derived from either exported phytoplankton or benthic

658   mats (Vairavamurthy et al., 1995). Unfortunately, in these dry-gas-window shales, we do not observe any

659   systematic distinction in kerogen S speciation (by XAS) between [34]S-depleted and [34]S-enriched kerogens,

660   because any speciation-based evidence for different source materials has been lost to diagenesis. However,

661   biogenic organic S was likely a smaller component of Mesoproterozoic kerogens than modern kerogens for

662   two reasons. First, amino acids, some of which are S-bearing, were likely to have been in especially high

663   demand as a fixed nitrogen source in a largely anoxic, denitrifying ocean (Michiels et al., 2017). And

664   second, relatively recalcitrant organic sulfate esters, such as the algal exudate fucoidan, were presumably

665   less abundant because they are primarily produced by eukaryotes, which were present in relatively low

666   abundances in the Mesoproterozoic (reviewed in Lyons et al., 2021). Therefore, although the potential for

667   biomass contributions cannot be excluded, we interpret Shale Valley kerogens primarily as records of the

668    $\delta^{34}S$ value of deeper sedimentary sulfides.

669

670   **4.4 Impacts of sulfurization on Proterozoic OM burial**

671   In many Mesozoic and more recent O_2-limited environments, there is a positive relationship between

672   sulfurization intensity (S:C ratio) and sedimentary OM concentrations (Boussafir et al., 1995; Van Kaam-

673   Peters et al., 1998; Raven et al., 2018, 2019). Despite the apparent relationship between environmental

674 redox conditions and OM sulfurization intensity, samples from the Arctic Bay Formation do not exhibit

675 clear relationships between indicators of sulfurization intensity (S:C ratios, kerogen S-isotopes, or Fe_{Py}/Fe_{HR}

676 ratios) and total organic carbon concentrations (Fig. S5 and S6). Instead, TOC has a broadly positive but

677 scattered relationship with Fe_{HR}/Fe_T (Figure 5b), indicating that anoxic conditions facilitate enhanced TOC

678 preservation via mechanisms other than sulfurization, such as oxygen scarcity. Although sulfurization was

679 not the primary driver of elevated OM concentrations in Arctic Bay Formation black shales, it did occur,

680 and it may have contributed to the preservation of sedimentary TOC. Additional paired organic S and pyrite

681 records from less mature black shales are needed to evaluate the significance of sulfurization for Proterozoic

682 OM burial more broadly.

683

684 Sulfurization may have a different relationship with quantitative OM burial in Proterozoic environments

685 than in well-studied Mesozoic environments for multiple reasons. Differences in sedimentary TOC content

686 may be especially sensitive to local primary productivity due to differences between Proterozoic and

687 Phanerozoic macronutrient cycles. Modern anoxic water columns have lower rates of OM remineralization

688 and phosphate regeneration than oxic locations (Van Mooy et al., 2002; Keil et al., 2016), which in turn

689 reduces the availability of phosphate to fuel primary productivity in upwelling zones. If the efficiency of

690 nutrient recycling in deep water were substantially reduced, Proterozoic primary producers could have been

691 much more dependent on local inputs of river-sourced phosphate than modern environments, where, in

692 contrast, 99% of phosphate supplied to primary producers is regenerated (Kipp and Stüeken, 2017; Laakso

693 and Schrag, 2019). By this logic, the elevated OM burial in Arctic Bay shales could primarily reflect

694 elevated local sources of phosphate to this semi-restricted basin.

695

696 The effects of anoxic deep water on OM preservation may have been at least partly offset by differences in

697 particle dynamics in Proterozoic versus Phanerozoic ecosystems. In modern marine systems, rapidly

698 sinking particles are a key link connecting rapid OM sulfurization and sediment OM burial. Eukaryotic

699 primary producers can generate large, ballasted, often polysaccharide-rich particles that transfer OM rapidly

700 to the seafloor (Alldredge and Silver, 1988; Engel et al., 2004) or even host internally reducing

701 microenvironments (Canfield et al., 2010; Raven et al., 2021a), and eukaryotic zooplankton contribute to

702 the rapidly sinking particle flux through vertical migration and fecal pellet production (Turner, 2015). The

703 microbial ecosystems of the Mesoproterozoic would have lacked these mechanisms for efficient transport

704 of OM to the seafloor (Logan et al., 1995). This difference would have increased particulate OM 'exposure

705 time' to water column conditions (Hartnett et al., 1998), which are typically less reducing and therefore

706 more energetically efficient for respiring OM than the sediments. Slower particle sinking thus increases the

707 likelihood of microbial degradation and defunctionalization of sinking particulate OM during transit and

708   decreases the odds of exposure of reactive OM to sulfidic conditions in surface sediments. OM preservation

709   may thus have been relatively sensitive to changes in particle formation and sinking rates in the water

710   column and less sensitive to chemical transformations like sulfurization in shallow sediments. In this

711   framework, OM burial in Arctic Bay shales could be enhanced by local inputs of terrigenous ballast

712   materials that facilitate rapid particle delivery to the sediments.

713

714   Additionally, bacterial and archaeal biomass may be less intrinsically susceptible to sulfurization than algal

715   biomass due to chemical differences in the compositions of their biomass and exudates. To date,

716   sulfurization experiments and environmental studies have focused primarily on algal biomass and

717   biomarkers like steroids (Gelin et al., 1998; Kok et al., 2000a, b; Raven et al., 2021b). Similar reactions are

718   likely to impact major components of bacterial and archaeal biomass but are less well understood.

719   Moreover, given the high OM S:C ratios observed in some Arctic Bay shales (up to ~5.2 mol%, with the

720   absence of pyrite confirmed by XAS), OM in this environment is clearly sulfurizable under the right

721   conditions. Therefore, although we do not observe a correlation between apparent sulfurization intensity

722   and TOC concentrations, sulfurization could have played a role in bulk OM preservation in locally sulfidic

723   Proterozoic environments, as it does in younger systems. Similarly, sulfurization could have contributed to

724   the enhanced preservation of specific components of sedimentary OM, including organic fossils or

725   biomarkers, especially in other, less mature Proterozoic rocks (Kohnen et al., 1991; Rosenberg et al., 2018;

726   Olcott et al., 2022; Tingle et al., 2023).

727

728

729   **5. CONCLUSIONS**

730

731   A global change in organic matter (OM) burial efficiency remains a leading hypothesis to reconcile carbon

732   mass balance throughout Earth history (Kipp et al., 2021), and enhanced OM sulfurization could be a

733   contributing mechanism to explain TOC-rich rocks of the mid-Proterozoic. We find clear evidence that

734   sulfurization occurred during early sedimentation and diagenesis of black shales under ferruginous-to-

735   sulfidic conditions in the late Mesoproterozoic Arctic Bay Formation, Borden Basin (~1.05 Ga).

736   Sulfurization at a relatively shallow site (Alpha River) was broadly concurrent with pyrite formation and

737   generated strongly [34]S-depleted OM. Although the organic sulfur content of these shales has been reduced

738   by thermal cracking during later diagenesis, kerogens that retained elevated S:C ratios are relatively rich in

739   disulfides, both indicating more intense sulfurization. Kerogen S:C ratios as high as 5.2 mol% suggest that

740   Mesoproterozoic biomass was similar to modern algal biomass in terms of its density of potentially

sulfurizable functional groups, and that it could have been strongly sulfurized under the right conditions, despite likely differences in major OM sources.

Although the shallow and deep sections of the Arctic Bay Formation have similar TOC and pyrite concentrations, conditions in the deeper basin site (Shale Valley) appear to have suppressed early diagenetic OM sulfurization. At that site, OM S-isotope compositions are relatively invariant and ^{34}S-enriched relative to coexisting pyrite, suggesting that ferruginous conditions in the water column drove sulfurization reactions deeper into the sediments.

Despite these observations, sulfurization intensity does not appear to be a primary driver of enhanced TOC concentrations in the Borden Basin, contrasting with observations from well-studied Mesozoic and more recent black shales. Instead, highly localized inputs of macronutrients and a phosphate-limited biosphere may have tightly coupled sedimentary TOC concentrations to local productivity levels. Alternatively, OM preservation efficiency may have been especially sensitive to processes impacting local particle fluxes and electron acceptor exposure times. Nevertheless, OM sulfurization did occur during sedimentation or early diagenesis, most notably during the deposition of TOC-rich shales at the shallower-water site, which means that sulfurization in this Mesoproterozoic environment retains the potential to enhance the preservation of specific components of OM (i.e., biomarkers, organic fossils) and to record valuable isotopic information about ancient biogeochemical cycles. Organic sulfur is an important but still poorly understood component of Earth's early sulfur cycle.

780

781   **Research Data**

782   All of the processed data discussed in this manuscript are available as part of the Supplemental Tables

783   associated with this article. Data are also available online at FigShare (link populated on manuscript

784   acceptance).

785

786   **Appendix A. Supplementary Material**

787   Supplementary Material for this manuscript includes six figures, details about the calculation of corrected

788   Fe_{Py}/Fe_{HR} ratios, and complete data tables. Figures show (1) XAS spectra for kerogens and whole rock

789   samples; (2) XAS standard spectra used in fits; (3) reconstructed iron speciation profiles; (4) relationships

790   between pyrite and sulfate; (5) the relationship between TOC concentrations and the ratio of highly reactive

791   iron to total iron; and (6) relationships between total organic carbon TOC concentrations and indicators of

792   organic matter sulfurization intensity.

793

794

795   **References**

796   Alldredge A. L. and Silver M. W. (1988) Characteristics, dynamics and significance of marine snow.
797   *Prog. Oceanogr.* **20**, 41–82.

798   Aller R. C., Madrid V., Chistoserdov A., Aller J. Y. and Heilbrun C. (2010) Unsteady diagenetic
799   processes and sulfur biogeochemistry in tropical deltaic muds: Implications for oceanic isotope
800   cycles and the sedimentary record. *Geochim. Cosmochim. Acta* **74**, 4671–4692.

801   Amrani A. and Aizenshtat Z. (2004a) Mechanisms of sulfur introduction chemically controlled: δ34S
802   imprint. *Org. Geochem.* **35**, 1319–1336.

803   Amrani A. and Aizenshtat Z. (2004b) Reaction of polysulfide anions with α,β unsaturated isoprenoid
804   aldehydes in aquatic media: simulation of oceanic conditions. *Org. Geochem.* **35**, 909–921.

805   Amrani A., Ma Q., Ahmad W. S., Aizenshtat Z. and Tang Y. (2008) Sulfur isotope fractionation during
806   incorporation of sulfur nucleophiles into organic compounds. *Chem. Commun.*, 1356.

807   Amrani A., Lewan M.D., Aizenshtat Z. (2005) Stable sulfur isotope partitioning during simulated
808   petroleum formation as determined by hydrous pyrolysis of Ghareb Limestone, Israel.
809   Geochimica et Cosmochimica Acta 69, 5317–5331.

810   Blackadar R. and Lemon R. (1963) Admirality Inlet area. *Baffin Isl. Dist. Frankl. Geol. Surv. Can. Mem.*
811   **328**, 84.

812   Blättler C. L., Bergmann K. D., Kah L. C., Gómez-Pérez I. and Higgins J. A. (2020) Constraints on
813   Meso- to Neoproterozoic seawater from ancient evaporite deposits. *Earth Planet. Sci. Lett.* **532**,
814   115951.

815   Bontognali T. R. R., Sessions A. L., Allwood A. C., Fischer W. W., Grotzinger J. P., Summons R. E. and
816   Eiler J. M. (2012) Sulfur isotopes of organic matter preserved in 3.45-billion-year-old
817   stromatolites reveal microbial metabolism. *Proc. Natl. Acad. Sci.* **109**, 15146–15151.

818   Boussafir M., Gelin F., Lallier-Vergès E., Derenne S., Bertrand P. and Largeau C. (1995) Electron
819   microscopy and pyrolysis of kerogens from the Kimmeridge Clay Formation, UK: Source
820   organisms, preservation processes, and origin of microcycles. *Geochim. Cosmochim. Acta* **59**,
821   3731–3747.

822   Bradley A. S., Leavitt W. D., Schmidt M., Knoll A. H., Girguis P. R. and Johnston D. T. (2016) Patterns
823   of sulfur isotope fractionation during microbial sulfate reduction. *Geobiology* **14**, 91–101.

824   Brantley S. L., Holleran M. E., Jin L. and Bazilevskaya E. (2013) Probing deep weathering in the Shale
825   Hills Critical Zone Observatory, Pennsylvania (USA): the hypothesis of nested chemical reaction
826   fronts in the subsurface: Nested Reaction Fronts. *Earth Surf. Process. Landf.* **38**, 1280–1298.

827   Cai C., Lyons T. W., Sun P., Liu D., Wang D., Tino C. J., Luo G., Peng Y. and Jiang L. (2022) Enigmatic
828   super-heavy pyrite formation: Novel mechanistic insights from the aftermath of the Sturtian
829   Snowball Earth. *Geochim. Cosmochim. Acta* **334**, 65–82.

830   Canfield D. E. (1994) Factors influencing organic carbon preservation in marine sediments. *Chem. Geol.*
831   **114**, 315–329.

832   Canfield D. E. (1989) Reactive iron in marine sediments. *Geochim. Cosmochim. Acta* **53**, 619–632.

833   Canfield Donald E., Farquhar J. and Zerkle A. L. (2010) High isotope fractionations during sulfate
834   reduction in a low-sulfate euxinic ocean analog. *Geology* **38**, 415–418.

835   Canfield D. E., Raiswell R., Westrich J. T., Reaves C. M. and Berner R. A. (1986) The use of chromium
836   reduction in the analysis of reduced inorganic sulfur in sediments and shales. *Chem. Geol.* **54**,
837   149–155.

838   Canfield Don E., Stewart F. J., Thamdrup B., De Brabandere L., Dalsgaard T., Delong E. F., Revsbech N.
839   P. and Ulloa O. (2010) A Cryptic Sulfur Cycle in Oxygen-Minimum–Zone Waters off the
840   Chilean Coast. *Science* **330**, 1375–1378.

841   Chambers L. A., Trudinger P. A., Smith J. W. and Burns M. S. (1975) Fractionation of sulfur isotopes by
842   continuous cultures of *Desulfovibrio desulfuricans*. *Can. J. Microbiol.* **21**, 1602–1607.

843   Chandra A. P. and Gerson A. R. (2010) The mechanisms of pyrite oxidation and leaching: A fundamental
844   perspective. *Surf. Sci. Rep.* **65**, 293–315.

845 Chen C.-T. A., Lin C.-M., Huang B.-T. and Chang L.-F. (1996) Stoichiometry of carbon, hydrogen,
846   nitrogen, sulfur and oxygen in the particulate matter of the western North Pacific marginal seas.
847   *Mar. Chem.* **54**, 179–190.

848 Cole D. B., Reinhard C. T., Wang X., Gueguen B., Halverson G. P., Gibson T., Hodgskiss M. S. W.,
849   McKenzie N. R., Lyons T. W. and Planavsky N. J. (2016) A shale-hosted Cr isotope record of
850   low atmospheric oxygen during the Proterozoic. *Geology* **44**, 555–558.

851 Crockford P. W., Hayles J. A., Bao H., Planavsky N. J., Bekker A., Fralick P. W., Halverson G. P., Bui T.
852   H., Peng Y. and Wing B. A. (2018) Triple oxygen isotope evidence for limited mid-Proterozoic
853   primary productivity. *Nature* **559**, 613–616.

854 Crockford P. W., Kunzmann M., Bekker A., Hayles J., Bao H., Halverson G. P., Peng Y., Bui T. H., Cox
855   G. M., Gibson T. M., Wörndle S., Rainbird R., Lepland A., Swanson-Hysell N. L., Master S.,
856   Sreenivas B., Kuznetsov A., Krupenik V. and Wing B. A. (2019) Claypool continued: Extending
857   the isotopic record of sedimentary sulfate. *Chem. Geol.* **513**, 200–225.

858 Dale A. W., Brüchert V., Alperin M. and Regnier P. (2009) An integrated sulfur isotope model for
859   Namibian shelf sediments. *Geochim. Cosmochim. Acta* **73**, 1924–1944.

860 Derry L. A. (2015) Causes and consequences of mid-Proterozoic anoxia. *Geophys. Res. Lett.* **42**, 8538–
861   8546.

862 Diamond C. W. and Lyons T. W. (2018) Mid-Proterozoic redox evolution and the possibility of transient
863   oxygenation events eds. T. W. Lyons, M. L. Droser, K. V. Lau, and S. M. Porter. *Emerg. Top.*
864   *Life Sci.* **2**, 235–245.

865 Duda J.-P., König H., Reinhardt M., Shuvalova J. and Parkhaev P. (2021) Molecular fossils within
866   bitumens and kerogens from the ~ 1 Ga Lakhanda Lagerstätte (Siberia, Russia) and their
867   significance for understanding early eukaryote evolution. *PalZ* **95**, 577–592.

868 Eglinton T. I., Irvine J. E., Vairavamurthy A., Zhou W. and Manowitz B. (1994) Formation and
869   diagenesis of macromolecular organic sulfur in Peru margin sediments. *Org. Geochem.* **22**, 781–
870   799.

871 Engel A., Thoms S., Riebesell U., Rochelle-Newall E. and Zondervan I. (2004) Polysaccharide
872   aggregation as a potential sink of marine dissolved organic carbon. *Nature* **428**, 929–932.

873 Fakhraee M., Hancisse O., Canfield D. E., Crowe S. A. and Katsev S. (2019) Proterozoic seawater sulfate
874   scarcity and the evolution of ocean–atmosphere chemistry. *Nat. Geosci.* **12**, 375–380.

875 Fike D. A., Bradley A. S. and Rose C. V. (2015) Rethinking the Ancient Sulfur Cycle. *Annu. Rev. Earth*
876   *Planet. Sci.* **43**, 593–622.

877 Fustic M., Ardakani O., Jiang C., Turner E., Mort A., Sanei H., and others (2017) Preliminary petroleum
878   potential and organic matter characterization of the Mesoproterozoic upper Arctic Bay Formation
879   (black shale) at Shale Valley Central, Northern Baffin Island, Nunavut, Canada. In *Gussow*
880   *Geoscience Conference, Lake Louise, Alta., Oct* pp. 8–11.

881 Gelin F., Kok M. D., de Leeuw J. W. and Sinninghe Damsté J. S. (1998) Laboratory sulfurisation of the
882   marine microalga Nannochloropsis salina. *Org. Geochem.* **29**, 1837–1848.

883 Gibson T. M., Shih P. M., Cumming V. M., Fischer W. W., Crockford P. W., Hodgskiss M. S. W.,
884   Wörndle S., Creaser R. A., Rainbird R. H., Skulski T. M. and Halverson G. P. (2018) Precise age
885   of Bangiomorpha pubescens dates the origin of eukaryotic photosynthesis. *Geology* **46**, 135–138.

886 Gibson T. M., Wörndle S., Crockford P. W., Bui T. H., Creaser R. A. and Halverson G. P. (2019)
887   Radiogenic isotope chemostratigraphy reveals marine and nonmarine depositional environments
888   in the late Mesoproterozoic Borden Basin, Arctic Canada. *GSA Bull.* **131**, 1965–1978.

889 Gorjan P., Veevers J. J. and Walter M. R. (2000) Neoproterozoic sulfur-isotope variation in Australia and
890   global implications. *Precambrian Res.* **100**, 151–179.

891 Gu X., Heaney P. J., Reis F. D. A. A. and Brantley S. L. (2020) Deep abiotic weathering of pyrite.
892   *Science* **370**, eabb8092.

893 Hahn K. E. and Turner E. C. (2017) Composition and history of giant carbonate seep mounds,
894   Mesoproterozoic Borden Basin, Arctic Canada. *Precambrian Res.* **293**, 150–173.

895 Hahn K. E., Turner E. C., Babechuk M. G. and Kamber B. S. (2015) Deep-water seep-related carbonate
896   mounds in a Mesoproterozoic alkaline lake, Borden Basin (Nunavut, Canada). *Precambrian Res.*
897   **271**, 173–197.

898 Harrison A. G. and Thode H. G. (1958) Mechanism of the bacterial reduction of sulphate from isotope
899   fractionation studies. *Trans. Faraday Soc.* **54**, 84.

900 Hartgers W., Lopez J., Sinninghe Damste J., Reiss C., Maxwell J. R. and Grimalt, J J. (1997) Sulfur-
901   binding in recent environments: II. Speciation of sulfur and iron and implications for the
902   occurrence of organo-suifur compounds. *Geochim. Cosmochim. Acta* **61**, 4768–4788.

903 Hartnett H. E., Keil R. G., Hedges J. I. and Devol A. H. (1998) Influence of oxygen exposure time on
904   organic carbon preservation in continental margin sediments. *Nature* **391**, 572–575.

905 Hedges J. I. and Keil R. G. (1995) Sedimentary organic matter preservation: an assessment and
906   speculative synthesis. *Mar. Chem.* **49**, 81–115.

907 Hemingway J. D., Rothman D. H., Grant K. E., Rosengard S. Z., Eglinton T. I., Derry L. A. and Galy V.
908   V. (2019) Mineral protection regulates long-term global preservation of natural organic carbon.
909   *Nature* **570**, 228–231.

910 Hodgskiss M. S. W., Sansjofre P., Kunzmann M., Sperling E. A., Cole D. B., Crockford P. W., Gibson T.
911   M. and Halverson G. P. (2020) A high-TOC shale in a low productivity world: The late
912   Mesoproterozoic Arctic Bay Formation, Nunavut. *Earth Planet. Sci. Lett.* **544**, 116384.

913 Houghton J., Scarponi D., Capraro L. and Fike D. A. (2022) Impact of sedimentation, climate and sea
914   level on marine sedimentary pyrite sulfur isotopes: Insights from the Valle di Manche section
915   (Lower-Middle Pleistocene, southern Italy). *Palaeogeogr. Palaeoclimatol. Palaeoecol.* **585**,
916   110730.

917 Ingall E. D. and Cappellen P. V. (1990) Relation between sedimentation rate and burial of organic
918   phosphorus and organic carbon in marine sediments. *Geochim. Cosmochim. Acta* **54**, 373–386.

919 Jin Q. and Bethke C. M. (2005) Predicting the rate of microbial respiration in geochemical environments.
920   *Geochim. Cosmochim. Acta* **69**, 1133–1143.

921 Jin X., Wu J., Fang P., Zhang Z., Li M. and Zhong N. (2021) Kinetics and fate of organosulphur
922   compounds during the metagenesis stage of thermal maturation: Hydrous pyrolysis investigations
923   on dibenzothiophene. *Mar. Pet. Geol.* **130**, 105129.

924 Johnston D. T. (2005) Multiple sulfur isotope fractionations in biological systems: A case study with
925   sulfate reducers and sulfur disproportionators. *Am. J. Sci.* **305**, 645–660.

926 Johnston D. T., Wing B. A., Farquhar J., Kaufman A. J., Strauss H., Lyons T. W., Kah L. C. and Canfield
927   D. E. (2005) Active Microbial Sulfur Disproportionation in the Mesoproterozoic. *Science* **310**,
928   1477–1479.

929 Jorgensen B. B. (1979) A theoretical model of the stable sulfur isotope distribution in marine sediments.
930   *Geochim. Cosmochim. Acta* **43**, 363–374.

931 Kah L. C., Lyons T. W. and Chesley J. T. (2001) Geochemistry of a 1.2 Ga carbonate-evaporite
932   succession, northern Baffin and Bylot Islands: implications for Mesoproterozoic marine
933   evolution. *Precambrian Res.* **111**, 203–234.

934 Kah L. C., Lyons T. W. and Frank T. D. (2004) Low marine sulphate and protracted oxygenation of the
935   Proterozoic biosphere. *Nature* **431**, 834–838.

936 Kaplan I. R. and Rittenberg S. C. (1964) Microbiological Fractionation of Sulphur Isotopes. *J. Gen.*
937   *Microbiol.* **34**, 195–212.

938 Keil R. G., Neibauer J. A., Biladeau C., van der Elst K. and Devol A. H. (2016) A multiproxy approach to
939   understanding the "enhanced" flux of organic matter through the oxygen-deficient
940   waters of the Arabian Sea. *Biogeosciences* **13**, 2077–2092.

941 Kelemen S. R., Sansone M., Walters C. C., Kwiatek P. J. and Bolin T. (2012) Thermal transformations of
942   organic and inorganic sulfur in Type II kerogen quantified by S-XANES. *Geochim. Cosmochim.*
943   *Acta* **83**, 61–78.

944 Kennedy M. J., Löhr S. C., Fraser S. A. and Baruch E. T. (2014) Direct evidence for organic carbon
945   preservation as clay-organic nanocomposites in a Devonian black shale; from deposition to
946   diagenesis. *Earth Planet. Sci. Lett.* **388**, 59–70.

947 Kipp M. A., Krissansen-Totton J. and Catling D. C. (2021) High Organic Burial Efficiency Is Required to
948   Explain Mass Balance in Earth's Early Carbon Cycle. *Glob. Biogeochem. Cycles* **35**,
949   2020GB006707.

950 Kipp M. A. and Stüeken E. E. (2017) Biomass recycling and Earth's early phosphorus cycle. *Sci. Adv.* **3**,
951   eaao4795.

952 Knoll A. H. and Sperling E. A. (2014) Oxygen and animals in Earth history. *Proc. Natl. Acad. Sci.* **111**,
953   3907–3908.

954 Kohnen M. E. l., Sinninghe Damsté J. S., Kock-van Dalen A. c. and Jan W. D. L. (1991) Di- or
955   polysulphide-bound biomarkers in sulphur-rich geomacromolecules as revealed by selective
956   chemolysis. *Geochim. Cosmochim. Acta* **55**, 1375–1394.

957 Kohnen M. E. L., Sinninghe Damsté J. S., Ten Haven H. L., kock.-Van Dalen A. C., Schouten S. and De
958   Leeuw J. W. (1991) Identification and geochemical significance of cyclic di-and trisulphides with
959   linear and acyclic isoprenoid carbon skeletons in immature sediments. *Geochim. Cosmochim.*
960   *Acta* **55**, 3685–3695.

961 Kok M. D., Rijpstra W. I. C., Robertson L., Volkman J. K. and Sinninghe Damstéé J. S. (2000a) Early
962   steroid sulfurisation in surface sediments of a permanently stratified lake (Ace Lake, Antarctica).
963   *Geochim. Cosmochim. Acta* **64**, 1425–1436.

964 Kok M. D., Schouten S. and Sinninghe Damsté J. S. (2000b) Formation of insoluble, nonhydrolyzable,
965   sulfur-rich macromolecules via incorporation of inorganic sulfur species into algal carbohydrates.
966   *Geochim. Cosmochim. Acta* **64**, 2689–2699.

967 Kunzmann M., Bui T. H., Crockford P. W., Halverson G. P., Scott C., Lyons T. W. and Wing B. A.
968   (2017) Bacterial sulfur disproportionation constrains timing of Neoproterozoic oxygenation.
969   *Geology* **45**, 207–210.

970 Laakso T. A. and Schrag D. P. (2019) A small marine biosphere in the Proterozoic. *Geobiology* **17**, 161–
971   171.

972 Leavitt W. D., Halevy I., Bradley A. S. and Johnston D. T. (2013) Influence of sulfate reduction rates on
973   the Phanerozoic sulfur isotope record. *Proc. Natl. Acad. Sci.* **110**, 11244–11249.

974 Li C., Love G. D., Lyons T. W., Fike D. A., Sessions A. L. and Chu X. (2010) A Stratified Redox Model
975   for the Ediacaran Ocean. *Science* **328**, 80–83.

976 Li X., Gilhooly W. P., Zerkle A. L., Lyons T. W., Farquhar J., Werne J. P., Varela R. and Scranton M. I.
977   (2010) Stable sulfur isotopes in the water column of the Cariaco Basin. *Geochim. Cosmochim.*
978   *Acta* **74**, 6764–6778.

979 Liu J., Antler G., Pellerin A., Izon G., Dohrmann I., Findlay A. J., Røy H., Ono S., Turchyn A. V., Kasten
980   S. and Jørgensen B. B. (2021) Isotopically "heavy" pyrite in marine sediments due to high
981   sedimentation rates and non-steady-state deposition. *Geology* **49**, 816–821.

982 Logan G. A., Hayes J. M., Hieshima G. B. and Summons R. E. (1995) Terminal Proterozoic
983   reorganization of biogeochemical cycles. *Nature* **376**, 53–56.

984 Long D. G. F. and Turner E. C. (2012) Tectonic, sedimentary and metallogenic re-evaluation of basal
985   strata in the Mesoproterozoic Bylot basins, Nunavut, Canada: Are unconformity-type uranium
986   concentrations a realistic expectation? *Precambrian Res.* **214–215**, 192–209.

987 Luo G., Ono S., Huang J., Algeo T. J., Li C., Zhou L., Robinson A., Lyons T. W. and Xie S. (2015)
988   Decline in oceanic sulfate levels during the early Mesoproterozoic. *Precambrian Res.* **258**, 36–47.

989 Lyons T. W. (1997) Sulfur isotopic trends and pathways of iron sulfide formation in upper Holocene
990   sediments of the anoxic Black Sea. *Geochim. Cosmochim. Acta* **61**, 3367–3382.

991   Lyons T. W., Diamond C. W., Planavsky N. J., Reinhard C. T. and Li C. (2021) Oxygenation, Life, and
992   the Planetary System during Earth's Middle History: An Overview. *Astrobiology* **21**, 906–923.

993   Lyons T. W., Luepke J. J., Schreiber M. E. and Zieg G. A. (2000) Sulfur geochemical constraints on
994   mesoproterozoic restricted marine deposition: lower Belt Supergroup, northwestern United
995   States. *Geochim. Cosmochim. Acta* **64**, 427–437.

996   Lyons T. W., Reinhard C. T. and Planavsky N. J. (2014) The rise of oxygen in Earth's early ocean and
997   atmosphere. *Nature* **506**, 307–315.

998   Mahoney C., März C., Buckman J., Wagner T. and Blanco-Velandia V.-O. (2019) Pyrite oxidation in
999   shales: Implications for palaeo-redox proxies based on geochemical and SEM-EDX evidence.
1000   *Sediment. Geol.* **389**, 186–199.

1001   Matrai P. A. and Eppley R. W. (1989) Particulate organic sulfur in the waters of the Southern California
1002   Bight. *Glob. Biogeochem. Cycles* **3**, 89–103.

1003   Michiels C. C., Darchambeau F., Roland F. A. E., Morana C., Llirós M., García-Armisen T., Thamdrup
1004   B., Borges A. V., Canfield D. E., Servais P., Descy J.-P. and Crowe S. A. (2017) Iron-dependent
1005   nitrogen cycling in a ferruginous lake and the nutrient status of Proterozoic oceans. *Nat. Geosci.*
1006   **10**, 217–221.

1007   Olcott A. N., Downen M. R., Schiffbauer J. D. and Selden P. A. (2022) The exceptional preservation of
1008   Aix-en-Provence spider fossils could have been facilitated by diatoms. *Commun. Earth Environ.*
1009   **3**, 94.

1010   Pasquier V., Fike D. A., Révillon S. and Halevy I. (2022) A global reassessment of the controls on iron
1011   speciation in modern sediments and sedimentary rocks: A dominant role for diagenesis. *Geochim.*
1012   *Cosmochim. Acta* **335**, 211–230.

1013   Pasquier V., Sansjofre P., Rabineau M., Revillon S., Houghton J. and Fike D. A. (2017) Pyrite sulfur
1014   isotopes reveal glacial−interglacial environmental changes. *Proc. Natl. Acad. Sci.* **114**, 5941–
1015   5945.

1016   Petsch S. T., Berner R. A. and Eglinton T. I. (2000) A field study of the chemical weathering of ancient
1017   sedimentary organic matter. *Org. Geochem.* **31**, 475–487.

1018   Planavsky N. J., McGoldrick P., Scott C. T., Li C., Reinhard C. T., Kelly A. E., Chu X., Bekker A., Love
1019   G. D. and Lyons T. W. (2011) Widespread iron-rich conditions in the mid-Proterozoic ocean.
1020   *Nature* **477**, 448–451.

1021   Planavsky N. J., Reinhard C. T., Wang X., Thomson D., McGoldrick P., Rainbird R. H., Johnson T.,
1022   Fischer W. W. and Lyons T. W. (2014) Low Mid-Proterozoic atmospheric oxygen levels and the
1023   delayed rise of animals. *Science* **346**, 635–638.

1024   Planavsky N. J., Slack J. F., Cannon W. F., O'Connell B., Isson T. T., Asael D., Jackson J. C., Hardisty
1025   D. S., Lyons T. W. and Bekker A. (2018) Evidence for episodic oxygenation in a weakly redox-
1026   buffered deep mid-Proterozoic ocean. *Chem. Geol.* **483**, 581–594.

1027   Poulton S. W. and Canfield D. E. (2005) Development of a sequential extraction procedure for iron:
1028   implications for iron partitioning in continentally derived particulates. *Chem. Geol.* **214**, 209–221.

1029 Poulton S. W. and Canfield D. E. (2011) Ferruginous Conditions: A Dominant Feature of the Ocean
1030   through Earth's History. *Elements* **7**, 107–112.

1031 Pye K. and Miller J. A. (1990) Chemical and biochemical weathering of pyritic mudrocks in a shale
1032   embankment. *Q. J. Eng. Geol.* **23**, 18.

1033 Raiswell R., Hardisty D. S., Lyons T. W., Canfield D. E., Owens J. D., Planavsky N. J., Poulton S. W.
1034   and Reinhard C. T. (2018) The iron paleoredox proxies: A guide to the pitfalls, problems and
1035   proper practice. *Am. J. Sci.* **318**, 491–526.

1036 Raven M. R., Adkins J. F., Werne J. P., Lyons T. W. and Sessions A. L. (2015) Sulfur isotopic
1037   composition of individual organic compounds from Cariaco Basin sediments. *Org. Geochem.* **80**,
1038   53–59.

1039 Raven M. R., Fike D. A., Bradley A. S., Gomes M. L., Owens J. D. and Webb S. A. (2019) Paired
1040   organic matter and pyrite δ34S records reveal mechanisms of carbon, sulfur, and iron cycle
1041   disruption during Ocean Anoxic Event 2. *Earth Planet. Sci. Lett.* **512**, 27–38.

1042 Raven M. R., Fike D. A., Gomes M. L., Webb S. M., Bradley A. S. and McClelland H.-L. O. (2018)
1043   Organic carbon burial during OAE2 driven by changes in the locus of organic matter
1044   sulfurization. *Nat. Commun.* **9**, 3409.

1045 Raven M. R., Keil R. G. and Webb S. M. (2021a) Microbial sulfate reduction and organic sulfur
1046   formation in sinking marine particles. *Science* **371**, 178–181.

1047 Raven M. R., Keil R. G. and Webb S. M. (2021b) Rapid, Concurrent Formation of Organic Sulfur and
1048   Iron Sulfides During Experimental Sulfurization of Sinking Marine Particles. *Glob. Biogeochem.*
1049   *Cycles* **35**.

1050 Raven M. R., Sessions A. L., Fischer W. W. and Adkins J. F. (2016) Sedimentary pyrite δ34S differs
1051   from porewater sulfide in Santa Barbara Basin: Proposed role of organic sulfur. *Geochim.*
1052   *Cosmochim. Acta* **186**, 120–134.

1053 Rosenberg Y. O., Kutuzov I. and Amrani A. (2018) Sulfurization as a preservation mechanism for the
1054   δ13C of biomarkers. *Org. Geochem.* **125**, 66–69.

1055 Rosenberg Y. O., Meshoulam A., Said-Ahmad W., Shawar L., Dror G., Reznik I. J., Feinstein S. and
1056   Amrani A. (2017) Study of thermal maturation processes of sulfur-rich source rock using
1057   compound specific sulfur isotope analysis. *Org. Geochem.* **112**, 59–74.

1058 Sarret G., Mongenot T., Connan J., Derenne S., Kasrai M., Michael Bancroft G. and Largeau C. (2002)
1059   Sulfur speciation in kerogens of the Orbagnoux deposit (Upper Kimmeridgian, Jura) by XANES
1060   spectroscopy and pyrolysis. *Org. Geochem.* **33**, 877–895.

1061 Scholz F. (2018) Identifying oxygen minimum zone-type biogeochemical cycling in Earth history using
1062   inorganic geochemical proxies. *Earth-Sci. Rev.* **184**, 29–45.

1063 Shawar L., Halevy I., Said-Ahmad W., Feinstein S., Boyko V., Kamyshny A. and Amrani A. (2018)
1064   Dynamics of pyrite formation and organic matter sulfurization in organic-rich carbonate
1065   sediments. *Geochim. Cosmochim. Acta* **241**, 219–239.

35

1066   Shawar L., Said-Ahmad W., Ellis G. S. and Amrani A. (2020) Sulfur isotope composition of individual
1067   compounds in immature organic-rich rocks and possible geochemical implications. *Geochim.*
1068   *Cosmochim. Acta* **274**, 20–44.

1069   Sim M. S., Bosak T. and Ono S. (2011) Large Sulfur Isotope Fractionation Does Not Require
1070   Disproportionation. *Science* **333**, 74–77.

1071   Sinninghe Damste J. S. and De Leeuw J. W. (1990) Analysis, structure and geochemical significance of
1072   organically-bound sulphur in the geosphere: State of the art and future research. *Org. Geochem.*
1073   **16**, 1077–1101.

1074   Sperling E. A. and Stockey R. G. (2018) The Temporal and Environmental Context of Early Animal
1075   Evolution: Considering All the Ingredients of an "Explosion." *Integr. Comp. Biol.* **58**, 605–622.

1076   Stolper D. A. and Keller C. B. (2018) A record of deep-ocean dissolved O2 from the oxidation state of
1077   iron in submarine basalts. *Nature* **553**, 323–327.

1078   Stüeken E. E., Kuznetsov A. B., Vasilyeva I. M., Krupenin M. T. and Bekker A. (2021) Transient deep-
1079   water oxygenation recorded by rare Mesoproterozoic phosphorites, South Urals. *Precambrian*
1080   *Res.* **360**, 106242.

1081   Suess E. (1973) Interaction of organic compounds with calcium carbonate-II. Organo-carbonate
1082   association in Recent sediments. *Geochim. Cosmochim. Acta* **37**, 2435–2447.

1083   Tingle K. E., Porter S. M., Raven M. R., Czaja A. D., Webb S. M. and Bloeser B. (2023) Organic
1084   preservation of vase-shaped microfossils from the late Tonian Chuar Group, Grand Canyon,
1085   Arizona, USA. *Geobiology*, gbi.12544.

1086   Trust B. A. and Fry B. (1992) Stable sulphur isotopes in plants: a review. *Plant Cell Environ.* **15**, 1105–
1087   1110.

1088   Turner E. C. and Kamber B. S. (2012) Arctic Bay Formation, Borden Basin, Nunavut (Canada): Basin
1089   evolution, black shale, and dissolved metal systematics in the Mesoproterozoic ocean.
1090   *Precambrian Res.* **208–211**, 1–18.

1091   Turner J. T. (2015) Zooplankton fecal pellets, marine snow, phytodetritus and the ocean's biological
1092   pump. *Prog. Oceanogr.* **130**, 205–248.

1093   Vairavamurthy A. (1998) Using X-ray absorption to probe sulfur oxidation states in complex molecules.
1094   *Spectrochim. Acta. A. Mol. Biomol. Spectrosc.* **54**, 2009–2017.

1095   Vairavamurthy M. A., Schoonen M. A. A., Eglinton T. I., Luther G. W. and Manowitz B. eds. (1995)
1096   *Geochemical Transformations of Sedimentary Sulfur.*, American Chemical Society, Washington,
1097   DC.

1098   Van Kaam-Peters H. M. E., Schouten S., Köster J. and Sinninghe Damstè J. S. (1998) Controls on the
1099   molecular and carbon isotopic composition of organic matter deposited in a Kimmeridgian
1100   euxinic shelf sea: evidence for preservation of carbohydrates through sulfurisation. *Geochim.*
1101   *Cosmochim. Acta* **62**, 3259–3283.

1102 Van Mooy B. A. S., Keil R. G. and Devol A. H. (2002) Impact of suboxia on sinking particulate organic
1103   carbon: Enhanced carbon flux and preferential degradation of amino acids via denitrification.
1104   *Geochim. Cosmochim. Acta* **66**, 457–465.

1105 van de Velde S. J., Reinhard C. T., Ridgwell A. and Meysman F. J. R. (2020) Bistability in the redox
1106   chemistry of sediments and oceans. *Proc. Natl. Acad. Sci.* **117**, 33043–33050.

1107 Webb S. M. (2005) SIXPack a Graphical User Interface for XAS Analysis Using IFEFFIT. *Phys. Scr.*,
1108   1011.

1109 Werne J. P., Lyons T. W., Hollander D. J., Formolo M. J. and Sinninghe Damsté J. S. (2003) Reduced
1110   sulfur in euxinic sediments of the Cariaco Basin: sulfur isotope constraints on organic sulfur
1111   formation. *Chem. Geol.* **195**, 159–179.

1112 Woltz C. R., Porter S. M., Agić H., Dehler C. M., Junium C. K., Riedman L. A., Hodgskiss M. S. W.,
1113   Wörndle S. and Halverson G. P. (2021) Total organic carbon and the preservation of organic-
1114   walled microfossils in Precambrian shale. *Geology* **49**, 556–560.

1115 Zaback D. A., Pratt L. M. and Hayes J. M. (1993) Transport and reduction of sulfate and immobilization
1116   of sulfide in marine black shales. *Geology* **21**, 141.

1117 Zerkle A. L., Kamyshny A., Kump L. R., Farquhar J., Oduro H. and Arthur M. A. (2010) Sulfur cycling
1118   in a stratified euxinic lake with moderately high sulfate: Constraints from quadruple S isotopes.
1119   *Geochim. Cosmochim. Acta* **74**, 4953–4970.

1120 Zhang Z., Li C., Cheng M., Algeo T. J., Jin C., Tang F. and Huang J. (2018) Evidence for Highly
1121   Complex Redox Conditions and Strong Water-Column Stratification in an Early Cambrian
1122   Continental-Margin Sea. *Geochem. Geophys. Geosystems* **19**, 2397–2410.

1123 (98 refs)